



ELSEVIER

Contents lists available at ScienceDirect

Journal of Computational Physics

www.elsevier.com/locate/jcp



Comprehensive numerical methodology for direct numerical simulations of compressible Rayleigh–Taylor instability



Scott J. Reckinger^{a,b,*}, Daniel Livescu^c, Oleg V. Vasilyev^a

^a Department of Mechanical Engineering, University of Colorado Boulder, 427 UCB, Boulder, CO 80309, 303-492-4717, USA

^b Civil Engineering Department, Montana State University, Bozeman, MT, 59717, USA

^c CCS-2 Computational Physics and Methods, Los Alamos National Laboratory, Los Alamos, NM 87545, USA

ARTICLE INFO

Article history:

Received 10 July 2014

Received in revised form 22 June 2015

Accepted 1 November 2015

Available online 4 November 2015

Keywords:

Rayleigh–Taylor instability

Compressible flow

Direct numerical simulations

Wavelet-based adaptive grid

Consistent initialization

Boundary conditions

ABSTRACT

An investigation of compressible Rayleigh–Taylor instability (RTI) using Direct Numerical Simulations (DNS) requires efficient numerical methods, advanced boundary conditions, and consistent initialization in order to capture the wide range of scales and vortex dynamics present in the system, while reducing the computational impact associated with acoustic wave generation and the subsequent interaction with the flow. An advanced computational framework is presented that handles the challenges introduced by considering the compressive nature of RTI systems, which include sharp interfacial density gradients on strongly stratified background states, acoustic wave generation and removal at computational boundaries, and stratification dependent vorticity production. The foundation of the numerical methodology described here is the wavelet-based grid adaptivity of the Parallel Adaptive Wavelet Collocation Method (PAWCM) that maintains symmetry in single-mode RTI systems to extreme late-times. PAWCM is combined with a consistent initialization, which reduces the generation of acoustic disturbances, and effective boundary treatments, which prevent acoustic reflections. A dynamic time integration scheme that can handle highly nonlinear and potentially stiff systems, such as compressible RTI, completes the computational framework. The numerical methodology is used to simulate two-dimensional single-mode RTI to extreme late-times for a wide range of flow compressibility and variable density effects. The results show that flow compressibility acts to reduce the growth of RTI for low Atwood numbers, as predicted from linear stability analysis.

© 2016 Elsevier Inc. All rights reserved.

1. Introduction

Rayleigh–Taylor instability (RTI) arises at perturbed interfaces, due to gravity-like body forces, accelerating fronts, or local differential motions, when the direction of the mean density gradient is opposite to acceleration [1,2]. RTI is observed in a wide range of astrophysical and atmospheric flows [3–5] and has drastic effects on many engineering systems of interest, such as inertial confinement fusion (ICF) [6,7]. Many of the systems where RTI naturally occurs involve strong compressibility effects. For example, RTI plays an important role in the flame propagation and development of ignition bubbles in type Ia supernovae [8], mixing and burning in X-ray bursts [9], development of supernova remnants [10], and ICF. Thus, a detailed understanding of the compressibility effects on the growth of RTI is necessary. Linear stability theory

* Corresponding author.

E-mail addresses: scott.reckinger@montana.edu (S.J. Reckinger), livescu@lanl.gov (D. Livescu), oleg.vasilyev@colorado.edu (O.V. Vasilyev).

has shown that there is no unique parameter characterizing compressibility [11]. Acoustic effects, material properties, and background stratification can all affect the instability growth, often in opposed ways. At late times, as the nonlinear effects become important, the number of these parameters is only expected to increase and their interactions become even more complicated. The combined effects of compressibility and large density gradients on the late-time behavior of RTI are not currently fully understood [5,12,13]. In addition, mixing itself generates pressure waves, while the piston-like motions of the bubbles and spikes can lead to the formation of strong shock waves [14].

Most RTI research has traditionally focused on the incompressible regime, even when compressible codes have been used. In such cases, the codes have been run near the incompressible limit with negligible background stratification, and the acoustic effects have been damped through the numerical scheme. For example, monotone integrated large eddy simulations (MILES) have been used to study the influence of initial conditions on the growth of RTI [15] and the self-similar growth factor [16]. Simulations of the compressible RTI system are much less common, but include studies that focus on Rayleigh–Taylor shock waves [14] and stratification effects on the turbulent mixing regime [17]. A recent review of numerical studies of compressible RTI considered the linear, nonlinear, and turbulent regimes [12]. There has not been a systematic investigation of the compressible RTI system to late-times using direct numerical simulations (DNS). Therefore, the full nature of the compressibility and stratification effects on the growth of RTI is unknown.

An accurate representation of the stratification, acoustic, and intrinsic compressibility effects involved in the compressible RTI system imposes strong requirements on the numerical scheme. Thus, the focus of this paper is to present an advanced computational framework that efficiently handles all of the issues associated with the compressible case. Attempting to perform numerical simulations of the compressible RTI system introduces a variety of additional complications, such as resolving the acoustic time scale, handling acoustic waves and RT shock waves at the boundaries, and performing computations over a vast range of density scales. In order to capture the late-time behavior, the simulations need to be performed in long vertical domains. If the background stratification is strong, as is typical for ICF, the density range can span orders of magnitude. In addition, vortices are generated continuously within the RT mixing layer and nonlinearly interact with one another to affect the late-time large-scale growth. For example, vortical interactions can lead to quadratic growth in the single-mode RTI case, which is very different than the “terminal velocity” that occurs when potential flow theory is applied [18]. While most RTI systems involve a multi-mode initial perturbation, there are instances when a single-mode type development occurs, for example the side wall bubble and spike in the tilted RTI configuration [19]. In addition, single-mode RT can expose any directional bias in the numerical algorithm, as the symmetries of the problem need to be maintained at all times [18]. Such directional bias in the numerical algorithm may be difficult to see in the multi-mode case, but usually leads to unphysical horizontal motions in the single-mode case. Therefore, as a more demanding test for the numerical algorithm, besides its own physical significance, in this paper the single-mode RTI configuration is considered.

To minimize the computational effort required for high resolution DNS, adaptive meshes can be utilized so that the resolution of the computational grid matches the local scale of the system. Thus, applying an adaptive multiresolution method efficiently resolves the required wide range of scales. A self-adaptive pseudospectral Chebyshev method has been utilized to study compressible RTI in a bounded container [20]. The method is limited in the types of boundaries that can be represented. In order to isolate the RTI growth from the effects of wave reflections at the boundaries, a special boundary treatment is presented using finite differences on a collocated grid. Thus, the growth of the instability can be observed until very late times. In addition, the use of a wavelet-based adaptive method for the simulation of complex fluid systems permits efficient use of computational resources, since high resolution simulations are performed only where small-scale structures are present in the flow. The wavelets allow the grid to dynamically adapt to the physical features in the flow as they evolve in time while maintaining a direct control of the error [21].

The paper is organized as follows. The equations that govern compressible RTI and the important nondimensional parameters are presented in Section 2. The next several sections address the numerical methodology proposed. Section 3 discusses the application of the wavelet-based adaptive method to DNS of compressible RTI. A consistent initialization for both the thermodynamic variables and the velocity field, such that the generation of acoustic waves is minimized and does not affect the instability growth, is presented in Section 4, while Section 5 presents two different boundary methodologies: a diffusion buffer zone that damps acoustic disturbances, and a characteristics-based non-reflecting boundary that removes the energy of acoustic waves from the stratified background. In Section 6, a dynamic time integration method is introduced that can be efficiently applied to highly nonlinear and potentially stiff convective–diffusive systems, such as compressible RTI. The comprehensive computational framework is then applied to simulations of two-dimensional single-mode RTI in Section 7. The simulations presented in this paper are all two-dimensional with single-mode perturbations, which act as a good test for the numerical algorithm by exposing any directional bias. However, the numerical methods are all easily extendable to three-dimensional domains with a multi-mode initialization. Specifically, the boundary conditions are general due to the mostly planar nature of the acoustic waves generated from the growth of compressible RTI. The validation of the methodology includes a resolution convergence study, simulations for a wide range of flow compressibility and variable density effects that remain symmetric well into late times, and a look at the flow compressibility effects for the small Atwood number case. Finally, conclusions and recommendations for future work are discussed in Section 8.

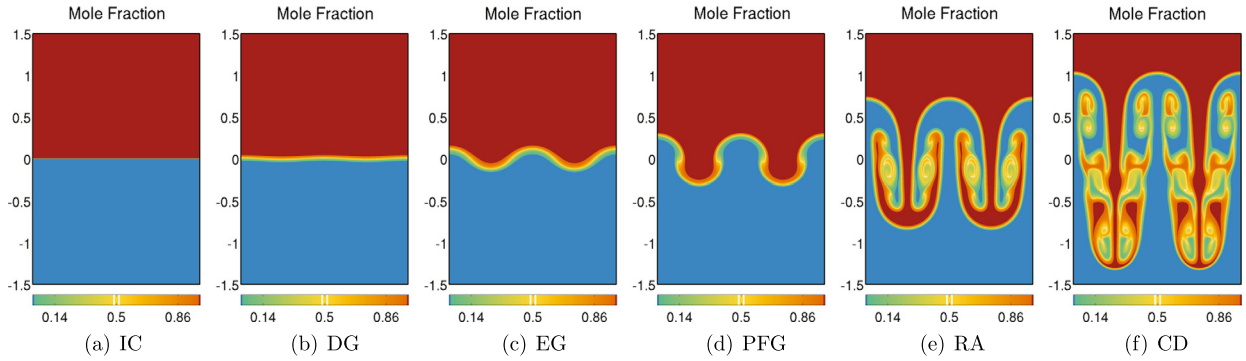


Fig. 1. The stages of incompressible RTI are shown using the mole fraction of the heavy fluid, labeled as: IC – initial conditions, DG – diffusive growth, EG – exponential growth, PFG – potential flow growth, RA – reacceleration, and CD – chaotic development.

2. Problem description

RTI occurs when a light fluid supports a heavier fluid in the presence of a gravity-like body force, an accelerating front, or local differential motions. At early times, small perturbations grow consistent with linear stability theory, which provides analytical solutions for the growth of the instability [22]. The linear growth rate depends on viscous, diffusive, compressibility, and finite density gradient effects, among others [11,23]. Whereas most theoretical and computational work on RTI focuses on the incompressible case, the extension of linear stability analysis to the compressible case has shown that the effects of compressibility on the early time growth rate cannot be represented by a single parameter. For initial conditions in thermal equilibrium, acoustic and stratification properties of the background flow are interrelated, with stratification itself playing an important role. The added complexity due to the effects of compressibility is expected to increase as the late time growth of RTI is investigated.

The growth stages for single-mode incompressible RTI, as shown in Fig. 1, have been studied in detail for the low Atwood number ($A = 0.04$) case [18]. Diffusion dominates early, while the perturbation begins to grow exponentially, consistent with linear stability theory. In the early nonlinear stages, the vorticity is still small and the instability growth can be described using potential flow theory or a simple buoyancy-drag model [24,25]. In the asymptotic limit of these models, where the buoyancy and drag effects are balanced, a constant bubble and spike velocity can be calculated as

$$V_{b/s} = \left[\frac{2A}{(1 \pm A)} \frac{g\lambda}{C_d} \right]^{1/2}, \quad (1)$$

where the drag coefficient is determined from the bubble terminal velocity relationships for the $A = 1$ limit, which gives $C_{d2D} = 6\pi$ and $C_{d3D} = 2\pi$. Until recently, this was called the “terminal” or asymptotic velocity, since it was believed to describe the late time behavior of single-mode RTI. However, as vorticity is generated by the Kelvin–Helmholtz instability on the sides of the bubbles and spikes, such a description becomes inadequate [18]. At late times, a chaotic development is observed, where numerous vortices interact with each other to produce rapid acceleration and deceleration of the bubbles and spikes. The late time acceleration fluctuates around a mean value such that the instability grows quadratically [18]. This differs from the long-held belief that the late-time instability growth is characterized by a constant velocity. If the viscous and diffusive effects are large enough to rapidly damp the vortices generated within the mixing layer, the growth is less affected by the vortex dynamics. For realistic flows where the Reynolds number is very large, vortices and the associated induced motions dominate the late-time behavior of RTI. The large-scale growth rate depends heavily on the vorticity generated at smaller scales, which highlights the need for high-resolution DNS. The vortices exist in localized regions of the flow, making the use of an adaptive grid beneficial. The computational framework presented here utilizes a dynamically adaptive grid, based on a representation of the solution using wavelets. This ensures sufficient resolution in the regions of vorticity generation, where the interface between the two materials is sharp and where strong gradients occur, e.g. around shock-waves.

2.1. Governing equations

RT systems are governed by the compressible Navier–Stokes, energy, and species mass fraction transport equations, where Y_1 corresponds to the mass fraction of the bottom fluid and Y_2 is the top fluid mass fraction. Assuming gases obeying the ideal gas equation of state, $p = \rho RT$, the full system of equations governing the flow of compressible viscous fluids of N_s ($l = 1, 2, \dots, N_s$) species is [5,26]

$$\frac{\partial \rho}{\partial t} + \frac{\partial \rho u_j}{\partial x_j} = 0, \quad (2)$$

$$\frac{\partial \rho u_i}{\partial t} + \frac{\partial \rho u_i u_j}{\partial x_j} = -\frac{\partial p}{\partial x_i} - \rho g_i + \frac{\partial \tau_{ij}}{\partial x_j}, \quad (3)$$

$$\frac{\partial \rho e}{\partial t} + \frac{\partial \rho e u_j}{\partial x_j} = -\frac{\partial p u_i}{\partial x_i} - \rho u_i g_i + \frac{\partial \tau_{ij} u_i}{\partial x_j} - \frac{\partial q_j}{\partial x_j} + \frac{\partial c_{p_l} T s_{jl}}{\partial x_j}, \quad (4)$$

$$\frac{\partial \rho Y_l}{\partial t} + \frac{\partial \rho Y_l u_j}{\partial x_j} = \frac{\partial s_{jl}}{\partial x_j}, \quad (5)$$

where ρ is the density, p is the pressure, T is the temperature, R is the gas constant, u_i is the velocity in the x_i direction, and the specific total energy is defined as

$$e = \frac{1}{2} u_i u_i + c_p T - \frac{p}{\rho}. \quad (6)$$

In the presentation of the governing equations, summation over repeated indices is assumed. The viscous stress, assuming Newtonian fluids, is defined as

$$\tau_{ij} = \mu \left(\frac{\partial u_i}{\partial x_j} + \frac{\partial u_j}{\partial x_i} - \frac{2}{3} \frac{\partial u_k}{\partial x_k} \delta_{ij} \right), \quad (7)$$

the heat flux is defined as

$$q_j = -k \frac{\partial T}{\partial x_j}, \quad (8)$$

and the species mass flux is defined as

$$s_{jl} = \rho D \frac{\partial Y_l}{\partial x_j}. \quad (9)$$

For the presentation of the current methodology, the baro-diffusion term is not included in the species mass flux formula. This term is necessary to satisfy the second law of thermodynamics and may be large at large density differences and strong background stratification [5]. However, simulations of compressible RTI do not usually consider this term. The numerical methodology proposed here is unaffected by the inclusion of the baro-diffusion term. Therefore, the physical importance of baro-diffusion, especially at high Atwood numbers when it is expected to be significant, will be addressed in a separate paper.

The gravitational acceleration is constant in the vertical, x_1 , direction, that is $g_i = g \delta_{i1}$. Fluid properties, such as the dynamic viscosity, μ , heat conduction coefficient, k , and mass diffusion coefficient, D , are typically mass-averaged quantities, defined as linear combinations of the individual species' properties using the mass fractions. For example, the mixture viscosity is defined as $\mu = \mu_l Y_l$, where summation over repeated indices is once again used. The RT system is composed of a heavy fluid lying on top of a lighter fluid in the vertical direction with the interface located at $x_1 = 0$. The requirement for instability is for the top fluid molar mass to be greater than that for the lower fluid, that is $W_1 < W_2$. The gas constant for the mixture can be calculated as

$$R = R_l Y_l = \mathcal{R} \frac{Y_l}{W_l}, \quad (10)$$

where \mathcal{R} is the universal gas constant. Consistent with the ideal gas assumption, the mixture specific heats at constant pressure and volume are calculated as mass averaged quantities, that is $c_p = c_{p_l} Y_l$.

2.2. Nondimensional parameters

The evolution of RTI involves an early-time linear growth regime, nonlinear growth of the bubble and spike structures, and chaotic growth at late-times characterized by a turbulent mixing layer. The molar mass ratio of the two fluids plays a major role in the shape and size of the structures and the growth rate of the instability. The Atwood number is a nondimensional quantity that represents the molar mass ratio, defined as

$$A = \frac{W_2 - W_1}{W_2 + W_1}. \quad (11)$$

In order to investigate the compressibility effects on RTI, a distinction is made between fluid compressibility characterized by the values of the ratios of the specific heats, γ_1 and γ_2 , and compressibility effects in response to the thermodynamic state of the system (flow compressibility). In order to isolate the flow compressibility effects, a Mach number is defined based on the gravity wave speed, $\sqrt{g\lambda}$, which characterizes the instability driving force, and the isothermal speed

of sound $a_0 = \sqrt{P_I/\rho_I}$, which removes the effects of the specific heats from the definition [11,27]. The definition of the isothermal Mach number is

$$M = \sqrt{\frac{\rho_I g \lambda}{P_I}}, \quad (12)$$

where the fluid density at the interface is given as

$$\rho_I = \frac{\mathcal{R}T_I}{P_I} \left(\frac{W_1 + W_2}{2} \right), \quad (13)$$

the reference pressure and temperature take on the background interfacial values P_I and T_I , and the reference length scale is given by the dominant perturbation wavelength, λ . For the single-mode system, λ represents the only wavelength present in the initial perturbation. For certain classes of initial conditions, such as the thermal equilibrium case, M also determines the vertical variations of the equilibrium density and pressure profiles. In these cases, it can be regarded, in addition, as a stratification parameter [12].

3. Parallel adaptive wavelet collocation method

Due to the nature of RTI, a wide range of scales must be resolved in order to perform accurate simulations. Large computational domains are necessary for performing simulations of RTI to late times, while small grid spacings are required near the interface for high Reynolds number flows. An adaptive method, where the resolution of the computational grid matches the local scale of the flow dynamics, can be used to alleviate the computational expense when resolving a wide range of scales. Wavelet-based simulations of turbulent flows are growing in popularity and success, which have been recently reviewed in Ref. [21]. The application of wavelets to the simulation of complex fluid systems range from turbulence modeling based on coherent vortex simulations [28] to simulations of shock-bubble interactions [29] and compressible reacting flow [30,31].

The Parallel Adaptive Wavelet Collocation Method (PAWCM) is an adaptive, multi-resolution method, which utilizes wavelets to locally adapt the numerical resolution during the evolution of complex flows [32–35]. Thus, localized structures are well-resolved while optimizing the use of computational resources. Unlike classical AMR techniques, PAWCM has the advantage of a threshold parameter that directly controls the error associated with the grid adaptation. PAWCM has been efficiently used for simulations of incompressible flows [36,37] and compressible inert and reactive flows [38,39]. The extension of PAWCM to simulations of RTI is promising due to the localized nature of the system.

PAWCM uses wavelet compression to dynamically adapt the grid to the local scale of the structures within the flow. The wavelets, which are localized in both wavenumber and physical space, are used as a set of basis functions to represent the flow variables. Wavelet compression is performed in wavelet space using wavelet coefficient thresholding, such that only the wavelets with significant magnitude are retained in the representation of the solution. The decomposition is given as

$$u_{\geq}(\mathbf{x}) = \sum_{\mathbf{k}} c_{\mathbf{k}}^0 \phi_{\mathbf{k}}^0(\mathbf{x}) + \sum_{j=0}^{+\infty} \sum_{\mu=1}^{2^j-1} \sum_{\mathbf{l}} d_{\mathbf{l}}^{\mu,j} \psi_{\mathbf{l}}^{\mu,j}(\mathbf{x}), \quad (14)$$

$|d_{\mathbf{l}}^{\mu,j}| \geq \epsilon \|u\|$

where u represents an arbitrary flow variable, $\phi_{\mathbf{k}}^j(\mathbf{x})$ are scaling functions at the coarsest level of resolution, $\psi_{\mathbf{l}}^{\mu,j}(\mathbf{x})$ are wavelet interpolating functions at varying levels of resolution, bold subscripts denote physical space indices, and the superscripts μ and j signify the family and level of resolution, respectively, of the wavelet or scaling function.

A wavelet coefficient, $d_{\mathbf{l}}^{\mu,j}$, will have a small value unless the function varies significantly on the scale j in the immediate vicinity of the wavelet $\psi_{\mathbf{l}}^{\mu,j}(\mathbf{x})$. For fields with isolated structures on a large-scale quiescent background, most of the wavelet coefficients are small. The wavelets associated with coefficients less than a prescribed threshold parameter, ϵ , can be discarded in representing the solution, while retaining only the significant wavelets gives an approximation with an error that is $O(\epsilon)$.

In order to simplify the computation of nonlinear terms, a wavelet collocation method is used, which ensures a one-to-one correspondence between grid points and wavelets. Derivatives are calculated at the corresponding local resolution using finite differences. Second-generation wavelets are used, which allow the order of the wavelets, and, thus, the order of the finite differences, to be easily varied [40]. Dynamic adaptation when solving evolution problems, such as the growth of RTI, is possible by adding an adjacent zone to the points associated with wavelets whose coefficients are significant. By adding the nearest neighbors of the significant wavelet coefficients in both position and scale, the computational grid contains points that could become significant during a time advancement step. A reconstruction check is also performed, ensuring that all the points required to perform the wavelet transforms are included on the mesh. When spatial derivatives are taken, ghost points are also added to the grid to maintain the desired order of the method.

For systems characterized by reflectional symmetry about a central axis, such as single-mode RTI, a symmetry check may also be applied. The symmetry check forces the grid to remain symmetric around the centerline of the bubbles and spikes.

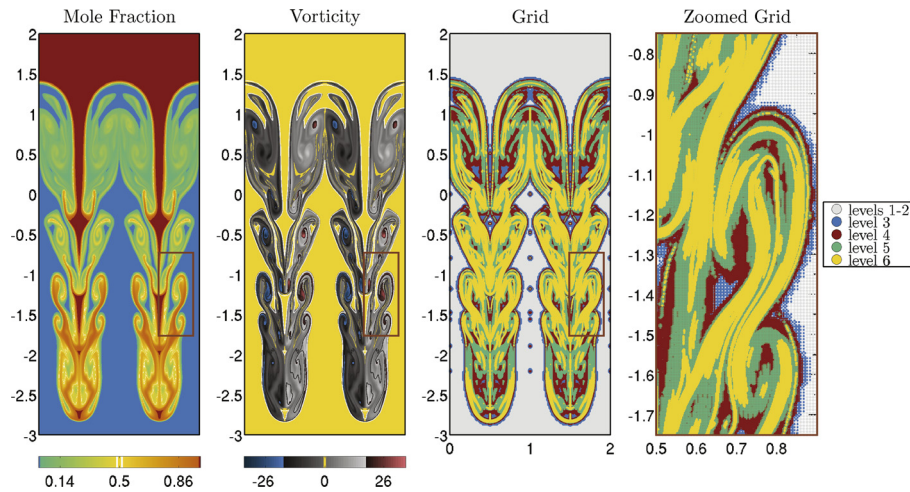


Fig. 2. Mole fraction, vorticity, and the associated adaptive grid for the late-time growth of RTI with $M = 0.3$ and $A = 0.3$. A zoomed view of the grid is given, corresponding to the brown boxes in the other figures.

Due to the intrinsic unstableness of the RTI system, the accumulation and nonlinear interaction of small numerical errors can lead to large-scale inaccuracies at late times, characterized by the unphysical introduction of secondary instabilities with arbitrary wavelength perturbations, which breaks the symmetries of the system. If a particular wavelet coefficient has a value slightly greater than the threshold parameter, ϵ , the wavelet is deemed significant and retained in the representation of the solution. However, the wavelet coefficient associated with its symmetric partner may have a value slightly less than ϵ due to small random computational fluctuations. Thus, the symmetric partner's wavelet, under normal circumstances, is deemed insignificant, and the wavelet coefficient is set to zero. For symmetric systems that are sensitive to secondary instabilities, such as single-mode RTI, the errors introduced by asymmetrically discarding insignificant wavelets can grow to affect the large-scale structures. Therefore, ensuring a symmetric grid removes this source of error and leads to stable simulations with longer durations. The solution itself is not forced to be symmetric, but only the grid. A half wavelength instability can be studied with mirror boundary conditions, which ensures the solution is symmetric. However, simulating the full wavelength acts as an accuracy check on the implementation of the numerical method.

The additional computational cost per grid point of PAWCM over standard non-adaptive methods (typically a factor around three to five) is negated in systems where small-scale structures occur in a small fraction of the domain. Applying PAWCM to simulations of RTI is a prime example where the compression of the grid is very high, since the mixing layer remains localized well into the nonlinear growth stage. Also, since a small percentage of the grid points are necessary to achieve high effective global resolutions, memory resources are used efficiently. The dynamic grid adaptation allows the efficient use of computational resources to resolve a wide range of scale structures as they evolve. A typical dynamically adapted grid with the symmetry check applied is shown in Fig. 2 for a late-time RTI simulation. For the simulation presented in the figure, the grid is generated by adapting on the mole fraction and vorticity, in addition to other important flow variables (such as velocity, strain rate, and mole fraction gradient). The effective global resolution is $32\,769 \times 2048$, yet only 7.5% of the points are used (5 003 157 points, 92.5% compression).

The largest challenge in parallelizing PAWCM lies in applying an effective load balancing procedure. Due to the dynamically adapting grid, using a geometric decomposition of the domain will inevitably lead to overloaded processors that act as a bottleneck for the entire simulation. The data are stored using a tree-like structure with tree roots starting at a sufficiently large level of resolution to shorten the tree traversing path and to minimize the size of the trees for data migration. For dynamic domain partitioning, the trees are considered to be the minimum quantum of data to be migrated between the processors. This allows for the efficient and fully automated handling of a non-simply connected partitioning of a computational domain. Dynamic load balancing is achieved through domain repartitioning during the grid adaptation step by reassigning trees to the appropriate processors to ensure approximately the same number of nodes on each processor. Further details on PAWCM can be found in Ref. [32].

4. Initialization

The initialization of the thermodynamic quantities and the velocity field for compressible RTI simulations must be derived directly from the governing equations to prevent strong acoustic wave generation at the interface. Multi-species systems that involve miscible fluids are intrinsically unsteady, since they will continually diffuse even when stably stratified. The presence of the enthalpy diffusion term in the energy equation leads to a non-zero time derivative at the interface, even if the system is initially at rest, and the formation of pressure waves. Thus, the initialization considers unstable immiscible modes, but special care is taken to minimize the generation of acoustic waves, which, if present, could strongly deviate

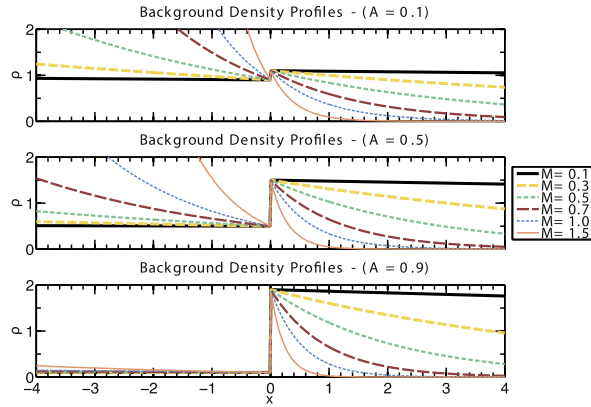


Fig. 3. Background density profiles at various M and A for the thermal equilibrium case.

the evolution of the perturbation from the growth predicted by linear stability theory, even when compressibility effects are small. The acoustic effects on the late-time growth of RTI are potentially even more severe. The initialization utilizes linear stability theory and the addition of a small dilatational velocity field, derived from the variable density limit, which approximately counteracts the enthalpy diffusion.

4.1. Thermodynamic initialization for compressible RTI

The RTI system is initialized with a hydrostatic background state, to which linear perturbation fields for density and pressure are added due to the interface perturbation. For example, pressure is initialized as

$$p(\mathbf{x}) = p^H(x_1) + p'(\mathbf{x}), \quad (15)$$

where $p^H(x_1)$ is the hydrostatic background pressure, which varies only in the vertical direction, and $p'(\mathbf{x})$ is the perturbation pressure field. Alternatively, the modes can also be superimposed such that no perturbation is required for the interface, density, or pressure, but a linear perturbation field for velocity is added.

The background state has a zero velocity field, representing a system at rest. Plugging $u_i = 0$ into the vertical momentum equation, the hydrostatic background state requires

$$\frac{\partial p^H}{\partial x_1} = -\rho^H g. \quad (16)$$

Assuming a background state in thermal equilibrium, $T^H(x_1) = T_0$, the solution for each fluid is

$$p_m^H(x_1) = P_I \exp\left(-\frac{g x_1}{R_m T_0}\right), \quad (17)$$

$$\rho_m^H(x_1) = \frac{P_I}{R_m T_0} \exp\left(-\frac{g x_1}{R_m T_0}\right), \quad (18)$$

where the subscript m denotes the fluid species.

The nondimensional version of the background equilibrium state is

$$p_{1,2}^{H*}(x_1) = \exp\left[-M^2(1 \mp A)x_1\right], \quad (19)$$

$$\rho_{1,2}^{H*}(x_1) = (1 \mp A) \exp\left[-M^2(1 \mp A)x_1\right]. \quad (20)$$

Fig. 3 shows the background density profiles for various M and A . For the thermal equilibrium case, M is also a measure of stratification and A is a measure of the interfacial density difference, which is made clear by comparing the various profiles. Additionally, the stratification within each fluid is strongly affected by A . At high values of A , the density profiles for the bottom fluid are largely unaffected by M , while the stratification in the top fluid is drastically affected by M . Note that in practical applications the initial density profile could be arbitrary; however, in general, these profiles will lead to an initial state which is out of equilibrium. For such problems, M is no longer a stratification parameter. Since out-of-equilibrium initial conditions cannot be addressed by linear stability analysis (e.g. the heat conduction term would prevent the time derivative in the energy equation to be zero), which is an important verification tool for numerical approaches, here we consider only initial conditions in thermal equilibrium as the base case for the compressible RTI problem. Cases with thermal out-of-equilibrium initial conditions will be addressed in future studies.

A single-mode perturbation is added to the hydrostatic background state consistent with linear stability theory [11]. The perturbation fields for the two-dimensional system are of the form

$$p'_m(x_1, x_2) = F_m(x_1) \exp(ikx_2 + nt), \quad (21)$$

$$\rho'_m(x_1, x_2) = G_m(x_1) \exp(ikx_2 + nt). \quad (22)$$

The x_1 -dependent functions are solved from the governing equations with the imposed solution from (21) and (22). For the fully compressible case, the growth rate, n , is given by an algebraic equation, which must be solved numerically [11]. The initial fields for pressure and density for each fluid are

$$p_m(\mathbf{x}) = p_m^H(x_1) + p'_m(\mathbf{x}), \quad (23)$$

$$\rho_m(\mathbf{x}) = \rho_m^H(x_1) + \rho'_m(\mathbf{x}), \quad (24)$$

where the perturbation fields are evaluated at $t = 0$.

When the material properties of two fluids prevent a homogeneous mixture, the system is characterized as immiscible, and the material interface is sharp. In this case, the pure fluid solutions are matched at the interface, and great care must be taken to accurately track the evolution of the material interface, e.g. [41]. Instead, of interest for this work is the miscible case, where the two fluids continually diffuse toward a homogeneous mixture, and defining an “interface” is arbitrary. If the region of partially mixed material is localized prior to perturbing the system, then the steepness of the “initial interface” must be resolved by the computational grid, to prevent the introduction of numerical noise. To ensure that the initial fields are well resolved, the interface is smoothed by setting the molar mass fraction to

$$X_1^H(x_1) = \frac{1}{2} \left[1 + \operatorname{erf} \left(\frac{x_1}{\delta} \right) \right], \quad (25)$$

where δ is the initial diffusion thickness of the interface. The error function is used in the molar mass fraction initialization because it is an exact solution to the diffusion equation. This initialization allows for an analytical solution of the smoothed background pressure and density fields,

$$p^H(x_1) = P_I \exp \left[\frac{-g}{R^H T_0} \left(x_1 - \frac{\delta^2}{2} \frac{\partial \ln R^H}{\partial x_1} \right) \right], \quad (26)$$

$$\rho^H(x_1) = \frac{p^H}{R^H T_0}. \quad (27)$$

These definitions represent smoothed fields because the gas constant takes on the local value according to the local mass fraction. Additionally, the extra smoothing term in the exponential is a direct result of the molar mass fraction initialization.

The perturbed interface is defined as $x_1 = \eta_I(x_2, x_3)$, which is imposed by setting the molar mass fraction to

$$X_1 = \frac{1}{2} \left[1 + \operatorname{erf} \left(\frac{x_1 - \eta_I(x_2, x_3)}{\delta} \right) \right]. \quad (28)$$

For the two-dimensional case,

$$\eta_I(x_2) = \eta_0 \exp(ikx_2), \quad (29)$$

where η_0 is the initial interface perturbation amplitude. The initial fields are smoothed at the interface using the contribution of the pure fluid solution to the smoothed hydrostatic background state. That is,

$$p = p_1 \frac{p^H}{p_1^H} \quad \text{and} \quad \rho = \rho_1 \frac{\rho^H}{\rho_1^H} \quad \text{for} \quad x_1 \geq \eta_I, \quad (30)$$

$$p = p_2 \frac{p^H}{p_2^H} \quad \text{and} \quad \rho = \rho_2 \frac{\rho^H}{\rho_2^H} \quad \text{for} \quad x_1 \leq \eta_I.$$

The perturbed initial temperature is then derived from the equation of state. Any potential jump in temperature at the interface is smoothed by numerically solving the diffusion equation for the temperature field. The smoothing is only done until the temperature field is well resolved. Any variation introduced from this final smoothing process is accounted for in the density field.

4.2. Velocity field initialization for compressible RTI

A zero velocity initialization is an obvious choice for the comparison of numerical simulations to experimental results, since most experiments attempt to start with static fluids. The zero initial velocity assumption for the equilibrium state is an intrinsic part of the linear stability analysis, which leads to consistent initial fields for the thermodynamic variables. However, when mixing is present at the interface, this initialization can generate pressure waves which will subsequently

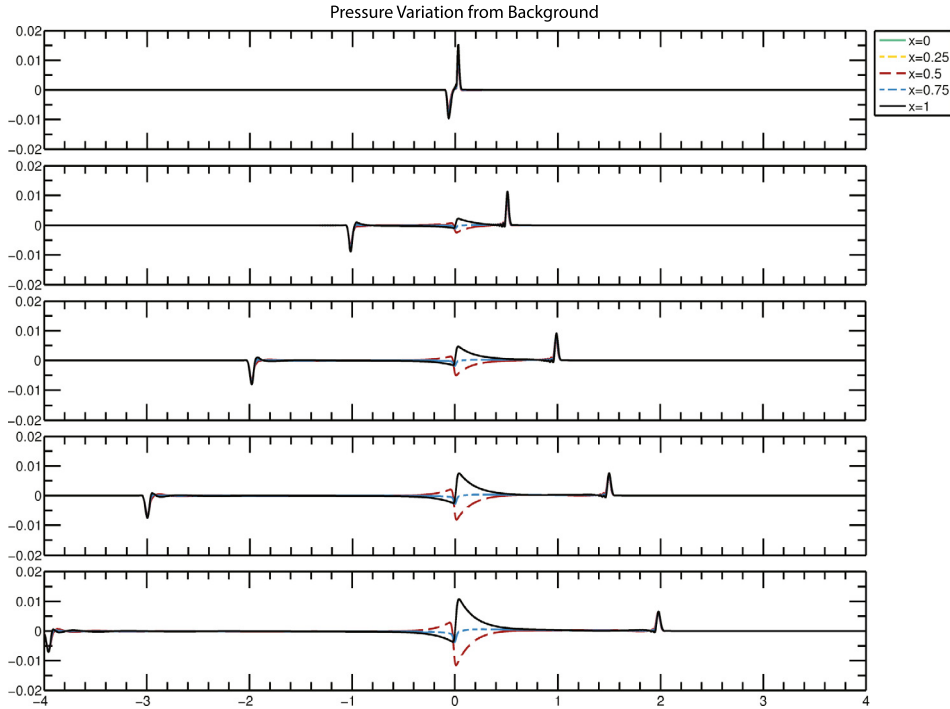


Fig. 4. The stationary, isothermal, hydrostatic background state leads to the generation of strong acoustic waves at the interface. The plots show the time evolution of vertical lines of the pressure variations from the background state, where time increases downward.

affect the solution. To explain this behavior, the governing equations can be written as

$$\frac{D\rho}{Dt} = -\rho \frac{\partial u_j}{\partial x_j}, \quad (31)$$

$$\frac{Du_i}{Dt} = -\frac{1}{\rho} \frac{\partial p}{\partial x_i} - g_i + \frac{1}{\rho} \frac{\partial \tau_{ij}}{\partial x_j}, \quad (32)$$

$$\begin{aligned} \frac{Dp}{Dt} = & -\gamma p \frac{\partial u_j}{\partial x_j} + (\gamma - 1) \tau_{ij} \frac{\partial u_i}{\partial x_j} + (\gamma - 1) \frac{\partial}{\partial x_j} \left[k \frac{\partial T}{\partial x_j} \right] \\ & + (\gamma - 1) D\rho \frac{\partial c_p}{\partial x_j} \frac{\partial T}{\partial x_j} + \gamma T \frac{\partial}{\partial x_j} \left[D\rho \frac{\partial R}{\partial x_j} \right], \end{aligned} \quad (33)$$

$$\frac{DR}{Dt} = \frac{1}{\rho} \frac{\partial}{\partial x_j} \left[D\rho \frac{\partial R}{\partial x_j} \right], \quad (34)$$

where D/Dt represents the material derivative. Applying the stationary ($u_i = 0$), isothermal ($T = T_0$), and hydrostatic ($\partial p/\partial x_i = -\rho g_i$) assumptions to the governing equations associated with the background state leads to $Dp/Dt \neq 0$. The nonzero time derivative arises because the species diffusion leads to a nonzero enthalpy diffusion term in the energy equation, which inevitably creates disturbances in the pressure field at the interface. If the initial gradients are steep enough, these disturbances can lead to the generation of relatively strong acoustic waves that propagate out from the initial interface. This effect was first observed by Cook [42] and further analyzed by Livescu [5]. Fig. 4 shows the generation and propagation of strong acoustic waves due to this out-of-equilibrium initialization.

The out-of-equilibrium effects in the initialization can be reduced by relaxing the stationary assumption of the initial state. In order to reduce the initial magnitude of $Dp/Dt = 0$ after applying only the isothermal ($T = T_0$) and hydrostatic ($\partial p/\partial x_i = -\rho g_i$) assumptions, and neglecting the viscous term, a balance is required for the remaining two terms,

$$\gamma p \frac{\partial u_j}{\partial x_j} = \gamma T \frac{\partial}{\partial x_j} \left[D\rho \frac{\partial R}{\partial x_j} \right]. \quad (35)$$

This leads to an equation for the divergence of velocity

$$\frac{\partial u_j}{\partial x_j} = \frac{1}{\rho R} \frac{\partial}{\partial x_j} \left[D\rho \frac{\partial R}{\partial x_j} \right] = \frac{\partial}{\partial x_j} \left[D \frac{\partial \ln R}{\partial x_j} \right] + D \frac{\partial \ln R}{\partial x_j} \frac{\partial \ln \rho R}{\partial x_j}. \quad (36)$$

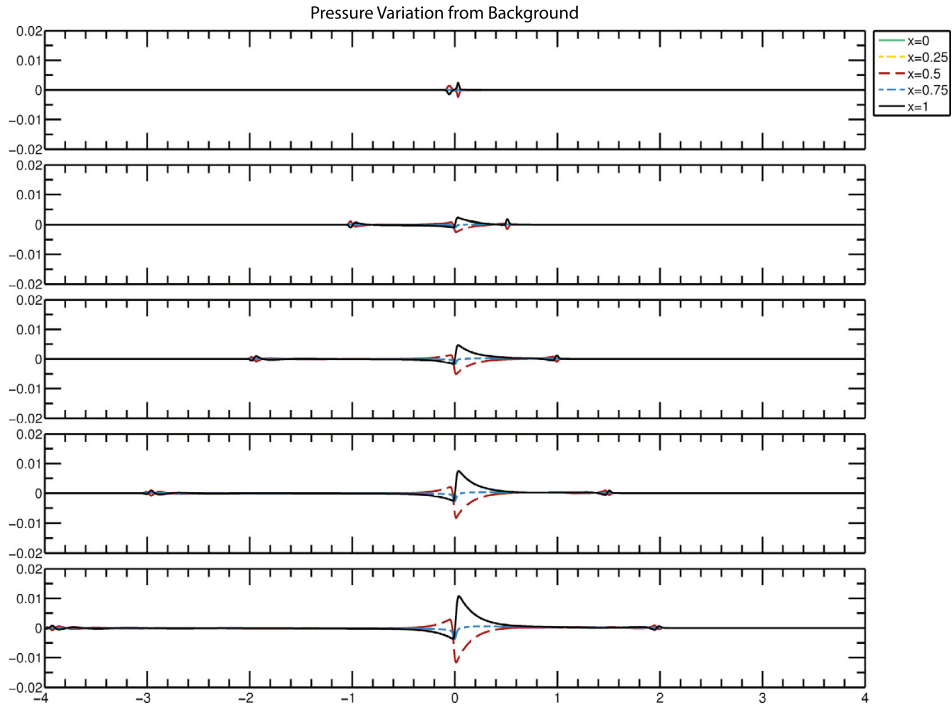


Fig. 5. The diffused, isothermal, hydrostatic background state leads to the generation of weak acoustic waves at the interface. The plots show the time evolution of vertical lines of the pressure variations from the background state, where time increases downward.

The last term typically has a small contribution, but may become significant for highly stratified cases with strong flow compressibility effects related to small P/T values. Neglecting this term leaves the following formula for the divergence of velocity

$$\frac{\partial u_j}{\partial x_j} = \frac{\partial}{\partial x_j} \left[D \frac{\partial \ln R}{\partial x_j} \right], \quad (37)$$

which is integrated to give the initial velocity field for minimizing the pressure disturbances at the interface,

$$u_i = D \frac{\partial \ln R}{\partial x_i}. \quad (38)$$

For variable density flows in the limit of incompressible pure fluids, mixing by species diffusion leads to non-zero divergence of velocity, which is equivalent to the result obtained here. The relationship was first derived by Joseph [43] for two miscible liquids and later derived from the compressible Navier–Stokes equations by Livescu [5]. Thus, the modified initialization represents a background state that is non-stationary but quasi-incompressible, diffused, isothermal, and hydrostatic around the interface. Away from the interface, the background state becomes consistent with the linear stability theory. Fig. 5 shows the generation and propagation of acoustic disturbances that are weak compared to the waves generated from the fully stationary background state shown in Fig. 4.

While the proposed initialization significantly reduces the pressure waves generated initially as the flow experiences a sudden perturbation, the acoustic generation is not completely eliminated. The elimination of these waves requires that the time derivatives of both pressure and density be simultaneously zero, which is not possible. The problem of reducing the amplitudes of these waves becomes much more complicated if the nonlinear contributions are considered in the governing equations. The solution proposed here is consistent with the incompressible (high speed of sound) limit and is relatively easy to implement. This solution also greatly reduces the interface position readjustment as the two fluids are suddenly brought into contact when the simulation is started. Eventually, the amplitudes of the acoustic waves generated through the initial conditions depend on all of the parameters of the problem: M , A , D , and the initial diffusive layer thickness, δ . The generation of pressure waves is not limited to the initial application of the perturbation and bringing the fluids into contact, but acoustic disturbances are continuously generated during the evolution of the instability due to the piston-like motions of bubbles and spikes [14]. All of these waves must be dealt with at the boundaries of the computational domain, in order to prevent wave reflection and contamination of the pure instability growth.

When adaptive grids are used for numerical simulations of RTI, additional computational resources must be used to resolve the propagation of the acoustic waves generated at the interface. Waves with higher amplitudes require higher resolution, and more resources are used to resolve the acoustics instead of the RTI growth. This can be observed in the adaptive

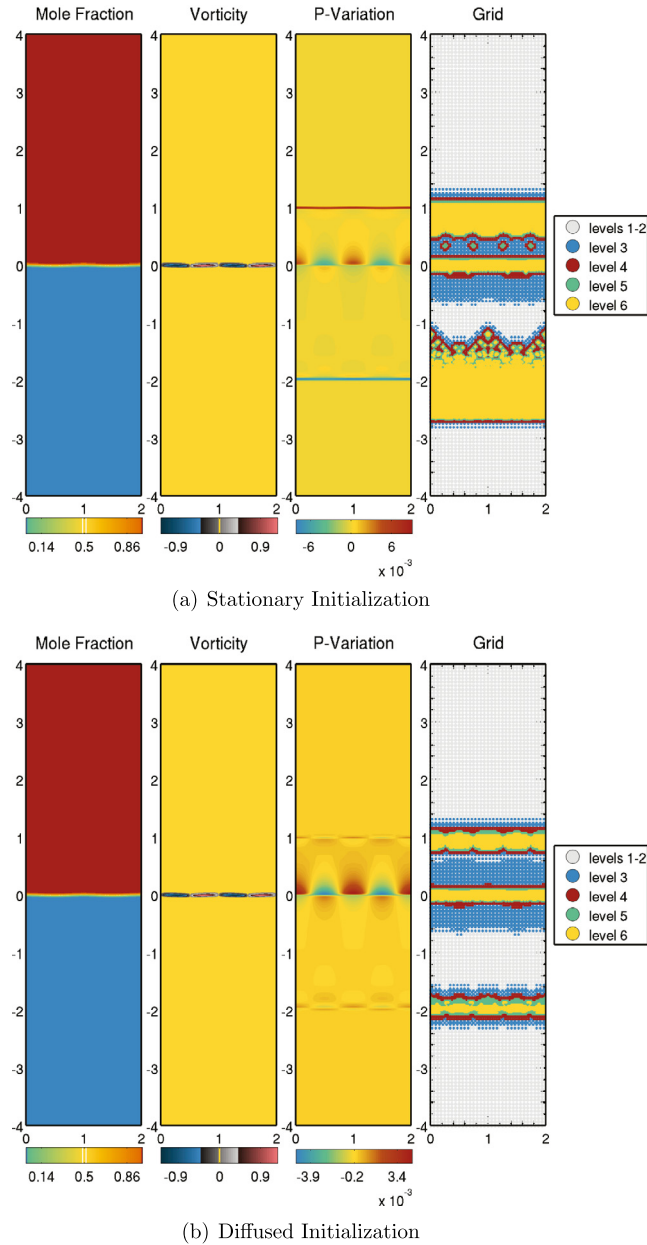


Fig. 6. Early time acoustic wave propagation for the two initializations. The grid for the stationary and diffused initializations encompass 116828 and 39537 active wavelets, respectively.

grids associated with the two initializations, shown in Fig. 6. The stationary initialization generates stronger acoustic waves and requires almost three times the number of active wavelets used to represent the diffused initialization case, where the acoustic generation is much weaker. The acoustic effect on the adaptive grid also has a longer duration for stronger acoustic waves. The adaptive grids at a later time, where the RTI growth is well into the linear regime, are shown in Fig. 7. The computational boundaries represent reflecting walls, such that the acoustic waves remain inside the computational domain and their late time effects can be observed. The grid continues to resolve the acoustics from the stationary initialization, whereas the diffused initialization case is only weakly adapting to the waves. Even at this late time, the zero initial velocity case uses 57% more points than the diffused initialization.

5. Boundary conditions

Simulations of systems lacking periodicity often require creative approaches near the computational boundaries in order to maintain high-order accuracy and stability of the solution. For compressible RTI, pressure waves are generated at the

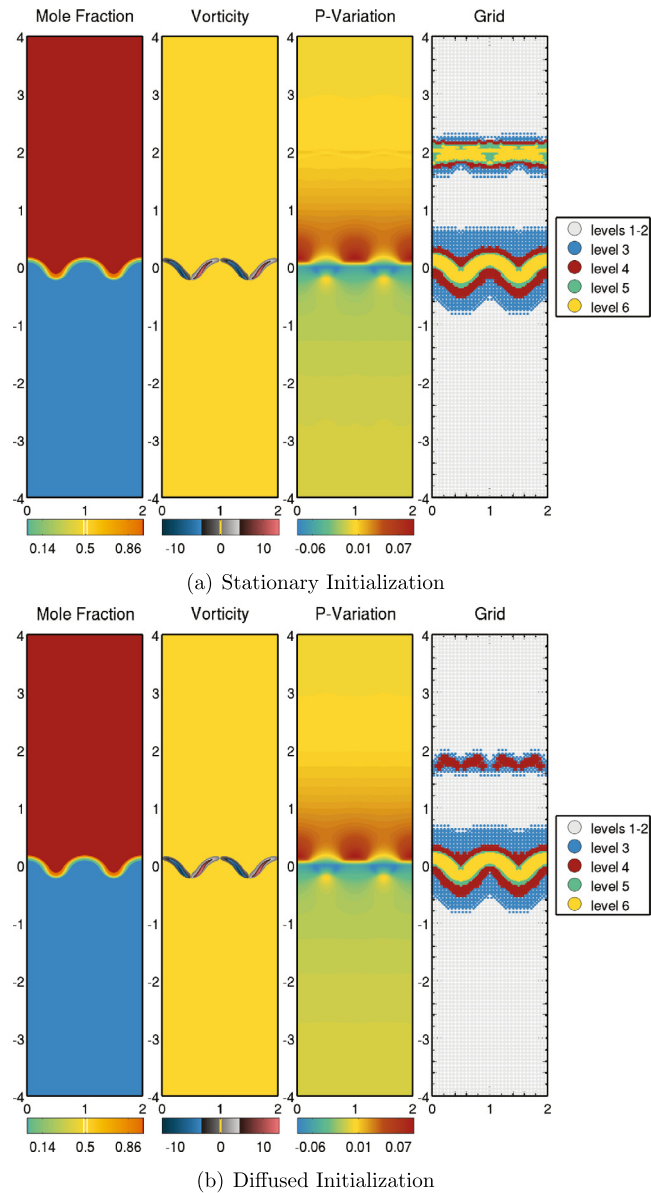


Fig. 7. Late time acoustic wave propagation for the two initializations showing the duration of acoustic effects on the adaptive grid. The grid for the stationary and diffused initializations have 32 173 and 20 465 active wavelets, respectively.

interface due to the initialization and the growth of the instability itself [14]. The acoustic waves travel outward and must be dealt with at the computational boundaries, where it is often desirable to have a complete removal of the waves. The goal is to represent a very large physical domain with a much smaller computational domain, which requires removing the energy of acoustic waves at the boundaries without affecting the background state. Thus, the stratification within each pure fluid adds an additional layer of complexity that must be accounted for when treating the computational boundaries.

Fig. 8 shows the background density and pressure profiles for a compressible RTI system with $A = 0.6$ and $M = 0.3118$. The A and M values are chosen such that the acoustic speed of the light fluid is exactly twice that of the heavy fluid. Fig. 9 shows the acoustic wave generation and propagation for the test case when shear-free slip walls are applied at the vertical boundaries. Vertical lines of the pressure variations from the background state are shown, with time increasing downward. Multiple vertical lines are displayed to show the planar nature of the wave. When slip wall boundary conditions are applied, the wave is free to reflect off the walls and interfere with the growth of the instability, thus highlighting the importance of properly handling the acoustic disturbances near the boundaries.

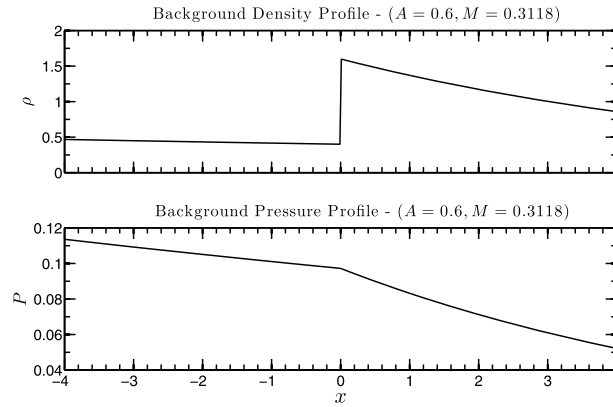


Fig. 8. Background density and pressure profiles for the $A = 0.6$ and $M = 0.3118$ case.

A review article on boundary conditions for compressible flow covers the evolution of nonreflecting boundary conditions (NRBCs) and wave-absorbing layers over the past decades [44]. NRBCs utilize analytical solutions of the system external to the computational domain at the computational boundaries. NRBCs work well when the flow near the boundary can be represented as a nearly uniform background state with small amplitude fluctuations, such as small amplitude acoustic waves. Absorbing layers are effective for a more general set of systems and work by damping disturbances, for example by increasing viscosity, in a localized region near the computational boundary. Special attention must be given to ensure wave reflections from the internal boundary of a wave-absorbing layer are minimized, typically by applying a gradual transition from small to large damping. Background stratification is not considered in the vast majority of the traditional NRBC and wave-absorbing layer methodologies. Thus, the traditional boundary treatments must be generalized for strongly stratified background states to be applicable for simulations of compressible RTI.

In this section, two distinct methodologies are presented for improving the near-boundary handling of acoustic waves with arbitrary stratification of the background state. The first approach involves applying a wave-absorbing buffer zone with increased viscous diffusion near the edge of the computational domain, such that perturbations from the background state are damped. The second approach is a NRBC that uses characteristic analysis to selectively remove the energy of acoustic waves at the computational boundaries. Both techniques are designed to simulate an infinite domain such that any pressure wave approaching a numerical boundary experiences minimal reflection and, thus, does not interact with and disturb the growth of the instability. Furthermore, both approaches allow arbitrary background stratification. The test case used in Fig. 9 is repeated for each boundary treatment to highlight the improved performance of each method.

5.1. Numerical diffusion buffer zone

Applying a numerical diffusion zone near the vertical edges of the computational domain does not remove the acoustic waves, but sufficiently reduces the intensity such that any wave reflection has negligible effect on the flow. The zone must be large enough for sufficient damping to occur. Since an adaptive grid is utilized, the computational cost of the buffer layer is negligible. Therefore, the buffer layer can be extended to extreme lengths to accommodate large damping.

The governing equations (2)–(5) are rewritten as

$$\frac{\partial \mathbf{U}}{\partial t} = \mathbf{F}(\mathbf{U}), \quad (39)$$

where all of the evolved variables are combined as $\mathbf{U} = [\rho, \rho \mathbf{u}, \rho e, \rho \mathbf{Y}]$, and $\mathbf{F}(\mathbf{U})$ represents all of the terms but the time derivatives. The fully conservative formulation of the diffusion buffer zone for a one-dimensional system is

$$\frac{\partial \mathbf{U}_i}{\partial t} = \mathbf{F}(\mathbf{U})_i + \left(\frac{2}{x_{i+1} - x_{i-1}} \right) \left[\xi_{i+1/2} \left(\frac{\mathbf{U}_{i+1}^P - \mathbf{U}_i^P}{x_{i+1} - x_i} \right) - \xi_{i-1/2} \left(\frac{\mathbf{U}_i^P - \mathbf{U}_{i-1}^P}{x_i - x_{i-1}} \right) \right], \quad (40)$$

where the subscripts signify the indices for the spatial grid, ξ is a function that accounts for the geometry and local strength of the numerical diffusion zone, and \mathbf{U}^P represents the perturbed quantities of the evolved variables from the background state, $\mathbf{U}^P = \mathbf{U} - \mathbf{U}^H$. Applying the numerical diffusion to the perturbation quantities allows spatially varying background fields, specifically those affected by the stratification intrinsic to compressible RTI.

Using smooth transitions for the diffusion buffer layer near the vertical boundaries, where the strength of the diffusive effects is gradually increased, allows the use of a simplified non-conservative scheme,

$$\frac{\partial \mathbf{U}}{\partial t} = \mathbf{F}(\mathbf{U}) + \nu_d \xi_d \frac{\partial^2 \mathbf{U}^P}{\partial x_j \partial x_j} - \sigma_b \xi_b \mathbf{U}^P. \quad (41)$$

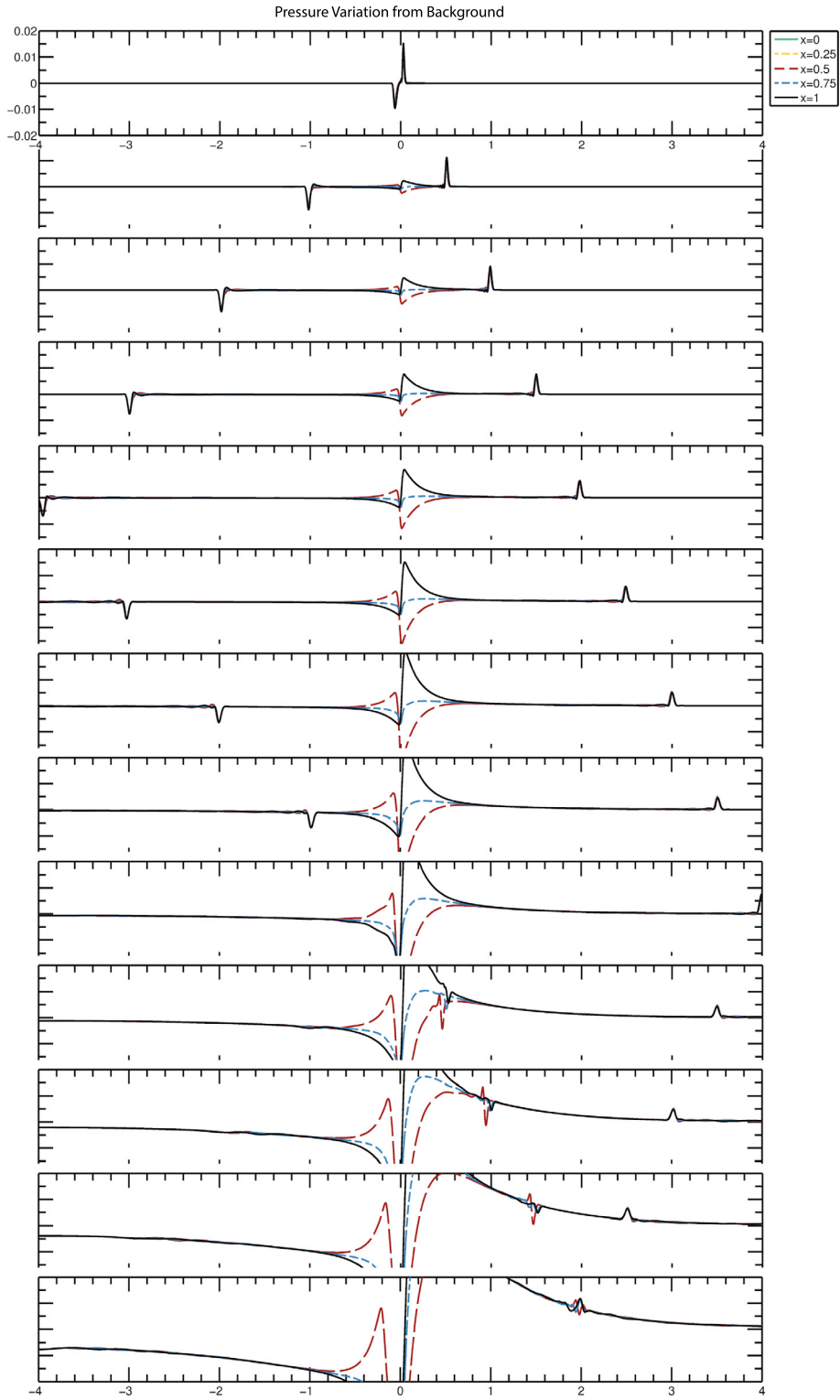


Fig. 9. Acoustic wave propagation with slip wall boundaries.

This formulation diffuses momentum and reduces kinetic energy in the buffer zone, but it is not fully conservative. The function $\xi_d(x_1)$ represents a mask function for the numerical diffusion zone. In the middle of the domain, $\xi_d = 0$, and no numerical diffusion is applied. Near the boundaries, ξ_d is gradually increased to one. The numerical diffusion coefficient, ν_d ,

is set locally to

$$\nu_d(x_1, x_2, x_3, t) = \left(2\Delta t \sum_{\alpha} \frac{1}{\Delta x_{\alpha}^2} \right)^{-1}, \quad (42)$$

where Δx_{α} changes is space and time as the grid dynamically adapts to the flow. Setting the diffusion coefficient in this way allows for maximum diffusion without introducing additional stability requirements. A low order derivative is used for the diffusion terms in order to reduce computational cost and to preserve monotonicity. The ‘L’ subscript on the second derivative signifies the low order nature of the discretized operator.

A Brinkman-type penalization term [45] is included to force the solution toward the background state within the Brinkman zone, represented by the Brinkman mask function, $\xi_b(x_1)$. In practice, it is common to use the same mask function for both the numerical diffusion zone and the Brinkman zone; that is, $\xi_b = \xi_d$. The forcing parameter, σ_b , is inversely proportional to the timescale of the damping. Large values of σ_b lead to a rapid driving of the solution to the background state at the expense of wave reflections at the boundaries of the Brinkman zone. At the opposite extreme, significantly small values of σ_b result in no forcing effect on the solution. An optimal amount of forcing for simulations of compressible RTI within the numerical diffusion zone is achieved using

$$\sigma_b = 0.25 \frac{c}{L}, \quad (43)$$

where c is the characteristic acoustic speed and L is a characteristic length scale. The local pure fluid acoustic speeds and length scales are applied, which leads to the final form of the forcing parameter,

$$\sigma_{b,\kappa} = 0.25 \sqrt{\frac{\gamma_{\kappa} \mathcal{R} T_0}{W_{\kappa} \lambda^2}}, \quad (44)$$

where summation over the repeated index, κ , is not assumed. Thus, the numerical diffusion zone at the bottom and top of the computational domain have different forcing parameters, $\sigma_{b,1}$ and $\sigma_{b,2}$ respectively.

A numerical diffusion buffer zone is applied to the test case and shown in Fig. 10. The diffusion layer mask, ξ_d , is gradually increased from zero to one between $3 < |x| < 3.25$, and the buffer zone takes full force, $\xi_d = 1$, where $3.25 < |x| < 4$. Shear-free slip wall conditions are applied at the top and bottom boundaries. When compared to the case without a diffusion zone, the acoustic waves are quickly and drastically damped upon entering the diffusion layer. The waves are not completely removed, but the amplitude is reduced significantly. This reduces the impact the acoustics have on the instability growth, while eliminating the computational cost of resolving the waves.

5.2. Characteristic boundary conditions for stratified flow

Poinsot and Lele developed a set of Navier–Stokes Characteristic Boundary Conditions (NSCBC) by analyzing the characteristic lines crossing the boundaries for the associated hyperbolic system, namely the Euler equations [46]. By considering the well-posedness of the Navier–Stokes equations, the method is extended to the full system of equations, including viscous terms. Thus, the propagation of waves from the Navier–Stokes equations are assumed to be associated only with the hyperbolic part. Since most simulations are performed for high Reynolds numbers, the approximation is well justified. A distinction is made between a physical boundary condition, one in which the condition specifies a known physical behavior, and a soft boundary condition, which is required by the numerical method without having an association with a physical attribute. The number of physical boundary conditions required for the well-posedness of the Navier–Stokes equations depends on the nature of the flow, whether subsonic or supersonic, and the type of boundary, such as a wall, inflow, or outflow. The optimal form for the required additional soft boundary conditions depends on the numerical implementation.

The NSCBC method using the Local One-Dimensional Inviscid (LODI) relations introduced by Poinsot and Lele [46] requires a modification to account for stratified background states, in order to be applied to simulations of compressible RTI. The classical LODI relations assume a constant background state, such that the stratification leads to unstable boundaries and strong wave reflections. Characteristic analysis is employed on the hyperbolic terms (viscous effects are not considered) corresponding to waves propagating in the x_1 direction [47]. Caution must be used when applying the LODI analysis to numerical simulations, since the full Navier–Stokes equations involve both viscous and tangential terms. The approximation is valid for sufficiently planar waves and small viscosity. The LODI relations have been successfully extended to non-planar, three-dimensional waves [45]. The LODI relations are extended for stratified flows in Appendix A, where pressure and density have been decomposed into the steady hydrostatic background state and the unsteady fields as follows,

$$p(\mathbf{x}, t) = p^H(x_1) + \check{p}(\mathbf{x}, t), \quad (45)$$

$$\rho(\mathbf{x}, t) = \rho^H(x_1) + \check{\rho}(\mathbf{x}, t). \quad (46)$$

The hydrostatic quantities are equivalent to the background state from the linear stability analysis. The relationship given in (16) holds true for p^H and ρ^H , and both are assumed constant with time. However, the hydrostatic fields vary with x_1

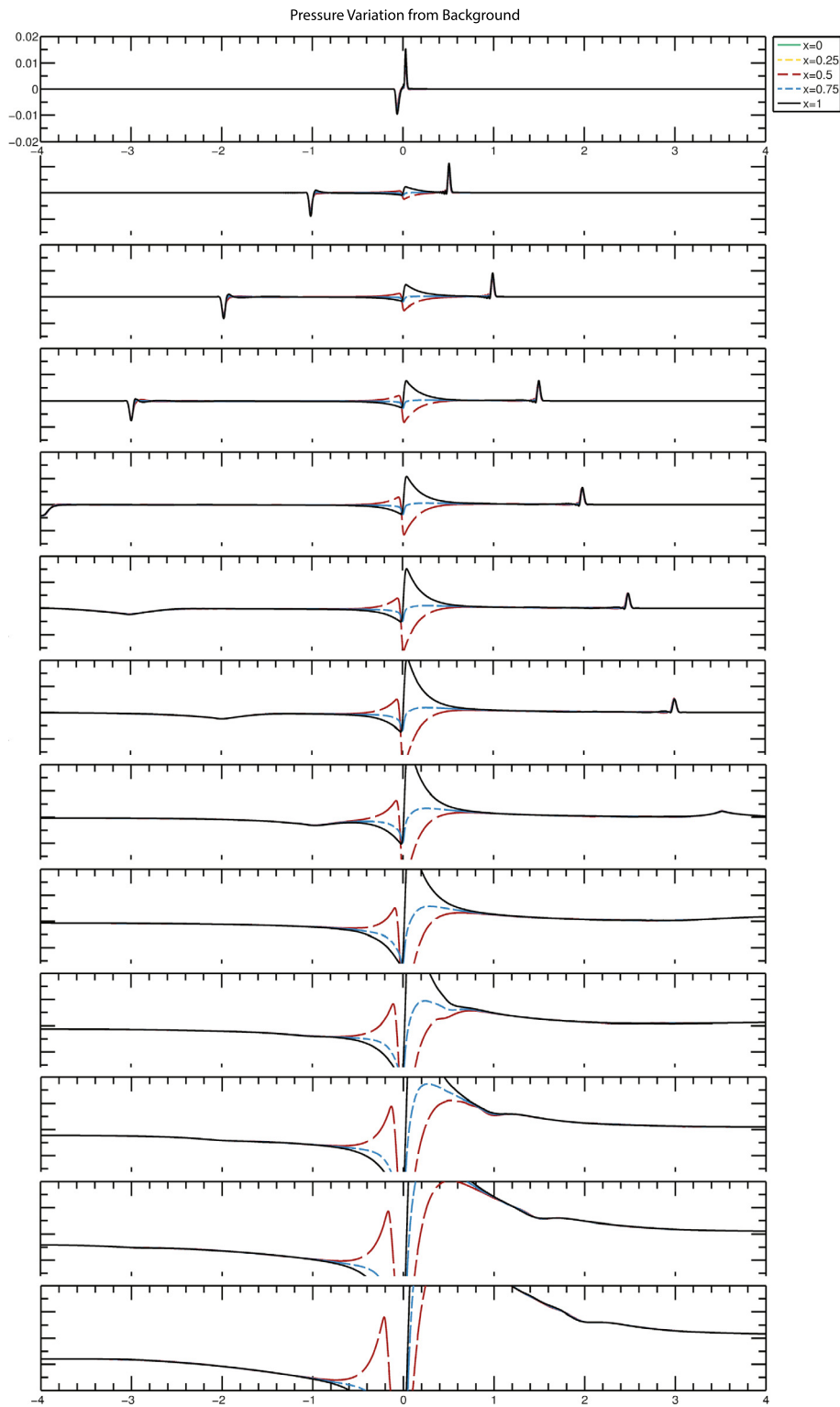


Fig. 10. Acoustic wave propagation with a diffusion buffer layer for $|x| > 3$.

everywhere, including near the boundaries. Therefore, the hydrostatic background state is removed from the pressure and density evolution terms before the characteristic equations are derived. The characteristic analysis of the one-dimensional inviscid problem is used to infer values for the wave amplitude variations in a multidimensional, viscous system. Extending

the stratified background, planar wave analysis for a d -dimensional velocity field and N_s fluid species, the LODI relations are

$$\frac{\partial \rho}{\partial t} + \frac{1}{2c^2}(\mathcal{I}_{N_v} + \mathcal{I}_1 + 2\mathcal{I}_2) = -u_1 \frac{\partial \rho^H}{\partial x_1}, \tag{47}$$

$$\frac{\partial u_1}{\partial t} + \frac{1}{2\rho c}(\mathcal{I}_{N_v} - \mathcal{I}_1) = \frac{\rho^H g}{\rho}, \tag{48}$$

$$\frac{\partial u_{(2:d)}}{\partial t} + \mathcal{I}_{(3:d+1)} = 0, \tag{49}$$

$$\frac{\partial p}{\partial t} + \frac{1}{2}(\mathcal{I}_{N_v} + \mathcal{I}_1) = \rho^H g u_1, \tag{50}$$

$$\frac{\partial Y_{(1:N_s)}}{\partial t} + \mathcal{I}_{(d+2:N_s+d+1)} = 0, \tag{51}$$

where the terms that have been added to the classical LODI analysis to account for stratification are colored blue (for clarity of the terms colored blue, the reader is referred to the web version of this article), $N_v = N_s + d + 2$ is the total number of evolved variables in the system, and the amplitude variation of the characteristic waves are

$$\mathcal{I}_1 = \lambda_1 \left(\frac{\partial \check{p}}{\partial x_1} - \rho c \frac{\partial u}{\partial x_1} \right), \tag{52}$$

$$\mathcal{I}_2 = \lambda_2 \left(c^2 \frac{\partial \check{\rho}}{\partial x_1} - \frac{\partial \check{p}}{\partial x_1} \right), \tag{53}$$

$$\mathcal{I}_{(3:d+1)} = \lambda_{(3:d+1)} \frac{\partial u_{2:d}}{\partial x_1}, \tag{54}$$

$$\mathcal{I}_{(d+2:N_s+d+1)} = \lambda_{(d+2:N_s+d+1)} \frac{\partial Y_{1:N_s}}{\partial x_1}, \tag{55}$$

$$\mathcal{I}_{N_v} = \lambda_{N_v} \left(\frac{\partial \check{p}}{\partial x_1} + \rho c \frac{\partial u}{\partial x_1} \right), \tag{56}$$

with characteristic velocities

$$\lambda_1 = u_1 - c, \tag{57}$$

$$\lambda_2 = \lambda_{(3:d+1)} = \lambda_{(d+2:N_s+d+1)} = u_1, \tag{58}$$

$$\lambda_{N_v} = u_1 + c. \tag{59}$$

The characteristic waves are grouped for convenience, with their true definitions in brackets, as

$$\mathcal{X}_1 = \frac{1}{2c^2}(\mathcal{I}_{N_v} + \mathcal{I}_1 + 2\mathcal{I}_2) \quad \left[= u_1 \frac{\partial \check{\rho}}{\partial x_1} + \rho \frac{\partial u_1}{\partial x_1} \right], \tag{60}$$

$$\mathcal{X}_2 = \frac{1}{2\rho c}(\mathcal{I}_{N_v} - \mathcal{I}_1) \quad \left[= u_1 \frac{\partial u_1}{\partial x_1} + \frac{1}{\rho} \frac{\partial \check{p}}{\partial x_1} \right], \tag{61}$$

$$\mathcal{X}_{(3:d+1)} = \mathcal{I}_{(3:d+1)} \quad \left[= u_1 \frac{\partial u_{(2:d)}}{\partial x_1} \right], \tag{62}$$

$$\mathcal{X}_{(d+2:N_s+d+1)} = \mathcal{I}_{(d+2:N_s+d+1)} \quad \left[= u_1 \frac{\partial Y_{(1:N_s)}}{\partial x_1} \right], \tag{63}$$

$$\mathcal{X}_{N_v} = \frac{1}{2}(\mathcal{I}_{N_v} + \mathcal{I}_1) \quad \left[= u_1 \frac{\partial \check{p}}{\partial x_1} + \rho c^2 \frac{\partial u_1}{\partial x_1} \right]. \tag{64}$$

The major advantage of casting the equations in this form is that, when considered near a computational boundary, the set of \mathcal{I}_k represents the amplitude variations of the characteristic waves crossing a boundary in the x_1 direction. The full system of equations governing the flow of compressible, viscous fluids of N_s species can then be written as

$$\frac{\partial \rho}{\partial t} + \left(\mathcal{X}_1 + u_1 \frac{\partial \rho^H}{\partial x_1} \right) + \sum_{n=2}^d \frac{\partial \rho u_n}{\partial x_n} = 0, \tag{65}$$

$$\begin{aligned} \frac{\partial \rho u_i}{\partial t} + u_i \left(\mathcal{X}_1 + u_1 \frac{\partial \rho^H}{\partial x_1} \right) + \left(\rho \mathcal{X}_{i+1} - \rho^H g_i \right) + \sum_{n=2}^d \frac{\partial \rho u_i u_n}{\partial x_n} = \\ - \frac{\partial p}{\partial x_i} (1 - \delta_{i1}) - \rho g_i + \frac{\partial \tau_{ij}}{\partial x_j}, \end{aligned} \tag{66}$$

$$\frac{\partial \rho e}{\partial t} + \frac{1}{2}(u_j u_j) \left(\mathcal{X}_1 + u_1 \frac{\partial \rho^H}{\partial x_1} \right) + \left(\rho u_j \mathcal{X}_{j+1} - \rho^H g_1 u_1 \right) \quad (67)$$

$$+ \frac{1}{\gamma - 1} \left(\mathcal{X}_{N_v} - \rho^H g_1 u_1 \right) + \sum_{n=2}^d \frac{\partial \rho e u_n}{\partial x_n} = - \sum_{n=2}^d \frac{\partial p u_n}{\partial x_n} - \rho u_i g_i + \frac{\partial \tau_{ij} u_i}{\partial x_j} - \frac{\partial q_j}{\partial x_j} + \frac{\partial c_{pl} T s_{jl}}{\partial x_j}, \quad (68)$$

$$\frac{\partial \rho Y_l}{\partial t} + Y_l \left(\mathcal{X}_1 + u_1 \frac{\partial \rho^H}{\partial x_1} \right) + \rho \mathcal{X}_{l+d+1} + \sum_{n=2}^d \frac{\partial \rho Y_l u_n}{\partial x_n} = \frac{\partial s_{jl}}{\partial x_j}. \quad (69)$$

The NSCBC are applied by first eliminating a conservation equation corresponding to each inviscid physical boundary condition. Then, the LODI relations (47)–(51) are used to express the wave amplitude variations, \mathcal{I}_κ , for the incoming waves in terms of the \mathcal{I}_κ for the outgoing waves. Lastly, extra viscous conditions required by the use of the Navier–Stokes equations are applied, and the remaining conservation equations (65)–(69) are solved on the boundaries. Two sample boundary types for subsonic flow are discussed in more detail in the following sections.

5.2.1. Adiabatic slip wall representation

Representing a slip wall using the LODI relations allows accurate handling of wave reflections for subsonic compressible flows. The single inviscid condition is that the normal velocity at the wall is zero, that is $u_1 = 0$. The only two wave amplitude variations that are not zero are related to one another through (48), which gives

$$\mathcal{I}_{N_v} - \mathcal{I}_1 = 2\rho^H g c, \quad (70)$$

one of which represents an incoming wave, the other an outgoing wave. The outgoing wave \mathcal{I}_κ is calculated from internal points and used to set the incoming wave amplitude variation from (70). The viscous conditions associated with an adiabatic slip wall require zero tangential viscous stresses, normal heat flux, and normal species flux. That is, at the wall,

$$\tau_{12} = \tau_{13} = q_1 = s_{1l} = 0. \quad (71)$$

The system is then evolved using the remaining conservation equations (65)–(69), not including the x_1 momentum equation.

5.2.2. Non-reflecting boundary conditions

Whereas a perfectly non-reflecting boundary condition is not likely possible for the general, stable computation of the Navier–Stokes equations, the NSCBC methodology offers an exact non-reflecting treatment of boundaries for one-dimensional systems that remains well-posed for multi-dimensional problems. For compressible systems with waves propagating through a non-reflecting boundary, the mean pressure must be controlled by setting a static pressure p_∞ and allowing small amplitude wave reflections. In this sense, the LODI relations are used for the application of partially-reflecting boundary conditions. By imposing a static pressure, none of the dependent variables are fixed on the boundaries, and all of the conservation equations must be solved. The incoming wave amplitude variation is $\mathcal{I}_{in} = \mathcal{I}_1$ for the top boundary and $\mathcal{I}_{in} = \mathcal{I}_{N_v}$ for the bottom boundary. In order to satisfy the condition of constant pressure at infinity, the incoming wave amplitude variation is set to

$$\mathcal{I}_{in} = K(p - p_\infty), \quad (72)$$

such that the pressure at the boundary evolves toward the static pressure over a timescale K^{-1} . The coefficient is treated as a constant for each outflow boundary as

$$K_\kappa = \sigma (1 - M_*^2) \frac{c_\kappa}{L}, \quad (73)$$

where $\kappa = 1$ for the top boundary, $\kappa = 2$ for the bottom boundary, L is a characteristic size of the domain, σ is a constant that measures the relative amount of wave reflection, and M_* is the maximum Mach number in the flow bounded by unity:

$$M_* = \min \left[\max \left(\left| \frac{u}{c} \right| \right), 1 \right]. \quad (74)$$

Setting $\sigma = 0$ leads to a perfectly non-reflecting boundary, which makes the system ill-posed. The optimal value in test cases was found to be $\sigma = 0.25$. Thus, the final form of the coefficient for simulations of the compressible RTI system investigated here is

$$K_\kappa = 0.25 \left(1 - M_*^2 \right) \sqrt{\frac{\gamma_\kappa \mathcal{R} T_0}{W_\kappa \lambda^2}}, \quad (75)$$

with no summation over κ .

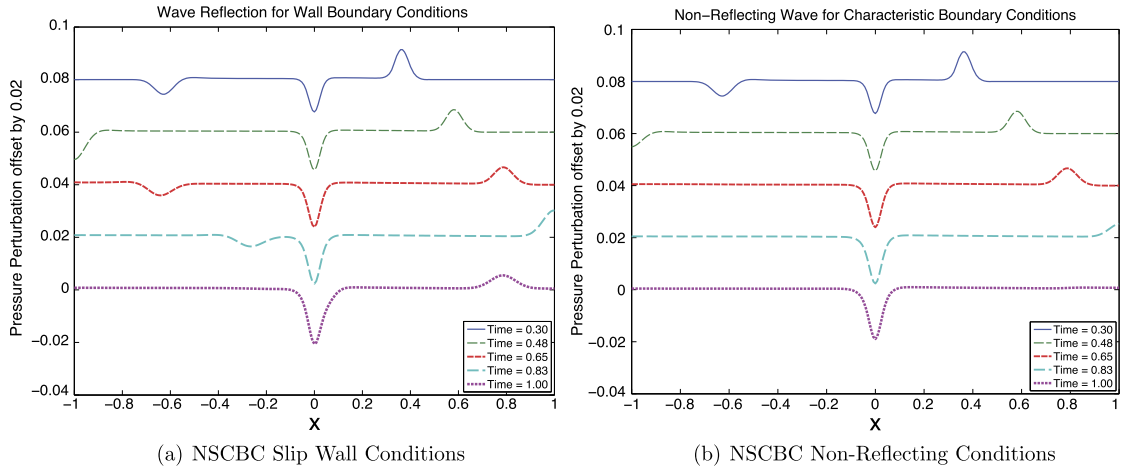


Fig. 11. The two characteristic-based boundary condition types are applied for the one-dimensional mixing in the RT unstable configuration. The pressure perturbation from the hydrostatic background is plotted at various times to show the acoustic waves approaching and reacting to the domain edges.

The viscous conditions require that the tangential stresses, normal heat flux, and normal species flux have zero spatial derivatives along x_1 . The conditions,

$$\frac{\partial \tau_{12}}{\partial x_1} = \frac{\partial \tau_{13}}{\partial x_1} = \frac{\partial q_1}{\partial x_1} = \frac{\partial s_{1l}}{\partial x_1} = 0 \quad (76)$$

are implemented directly into the system of equations by explicitly setting the derivatives to zero. The system is then evolved using all of the conservation equations (65)–(69).

5.2.3. Application of NSCBC to compressible RTI

Both the adiabatic slip wall and non-reflecting boundary conditions discussed in the previous sections can be implemented with the modified LODI conditions for stratified flow. For both boundary condition types, the well-posedness of the system is ensured by treating the flux terms consistent with the NSCBC methodology. Fig. 11 shows the two boundary condition types applied to the one-dimensional mixing of RT-unstable fluids. Acoustic waves are generated from the initial conditions due to the molecular mixing and travel outward towards the boundaries. The non-hydrostatic component of pressure is plotted at five times. Whereas the wave fully reflects with the modified characteristic slip wall condition, there is essentially no reflection when the non-reflecting modified characteristic conditions are applied, successfully simulating an infinite domain with a non-constant background pressure field.

The characteristics-based non-reflecting boundary conditions for stratified flows is applied to the test case and shown in Fig. 12. In comparison with the slip wall and diffusion buffer zone cases, the non-reflecting boundaries admit no appreciable wave reflection. The small additional computational cost required to use a non-reflecting boundary condition is outweighed by its success at simulating an infinite domain with stratified fluids. For dynamically adaptive methods, complete removal of the acoustics at the boundaries prevents unnecessary adaptation on the propagating waves, leading to an efficient use of computational resources.

6. Time integration schemes

When performing time-dependent numerical simulations of fluid systems such as RTI, there is no general time integration scheme that is optimal for all cases. An effective time discretization method depends on the nonlinearity of the governing equations, the diversity of terms in the equations, the stiffness of the system, stability requirements, and the required accuracy of the solution. Thus, different time integration schemes are optimal for different problems and parameter sets. Furthermore, various time discretization methods may be employed throughout a single simulation, as the evolution of the flow and the dynamically adaptive grid leads to temporal fluctuations of the stability requirements.

The use of a fully explicit time integration scheme, such as those presented in Appendix C, is unreasonable for high resolution simulations of a fluid system where viscous and diffusion effects are significant, due to strict stability requirements from the diffusion terms. Fully implicit schemes, such as those discussed in Appendix B, may also be inefficient due to the need to iterate on the nonlinear hyperbolic terms. A third option is to discretize each term individually in order to take full advantage of the benefits of implicit and explicit methodology, while eliminating many of the drawbacks. Implicit-explicit (IMEX) Runge–Kutta schemes combine diagonally implicit Runge–Kutta (DIRK) and fully explicit Runge–Kutta (ERK) schemes [48]. The hyperbolic and parabolic terms are grouped separately, such that $\mathbf{F}(\mathbf{U}) = \mathbf{H}(\mathbf{U}) + \mathbf{P}(\mathbf{U})$, and the generalized

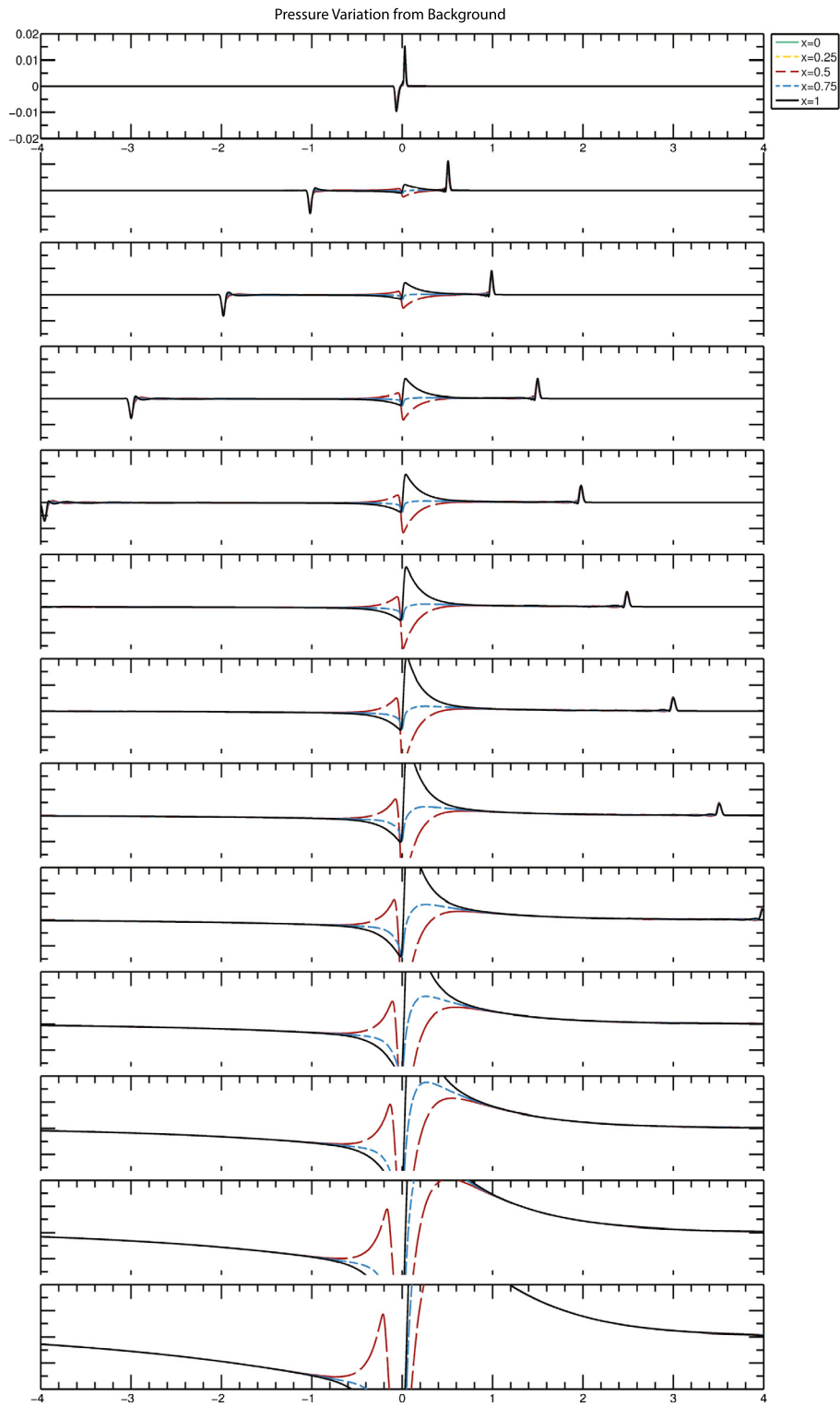


Fig. 12. Acoustic wave propagation with non-reflecting boundaries.

governing equations from (39) are rewritten as

$$\frac{\partial \mathbf{U}}{\partial t} = \mathbf{H}(\mathbf{U}) + \mathbf{P}(\mathbf{U}). \quad (77)$$

The hyperbolic part, $\mathbf{H}(\mathbf{U})$, corresponds to the convection, pressure gradient, and body force terms. The remaining diffusion terms make up the parabolic part, $\mathbf{P}(\mathbf{U})$. Systems with negligible diffusive effects ($\mathbf{P} \approx 0$) are generally nonlinear, but not too stiff. Conversely, diffusion dominated systems ($\mathbf{H} \approx 0$) tend to be highly stiff, but mostly linear. Thus, IMEX schemes use an ERK method for the discretization of $\mathbf{H}(\mathbf{U})$, and a DIRK method for $\mathbf{P}(\mathbf{U})$, while optimizing the DIRK attenuation properties and the combined stability regions. The required number of iterations is often small during the implicit steps of these IMEX schemes, especially when using efficient iterative solvers, such as the multilevel BiCGSTAB method performed on an adaptive grid while using PAWCM. However, since an implicit stage is more expensive than an explicit step, IMEX schemes are developed to reduce the number of implicit steps while maintaining the required order of accuracy.

The accuracy, attenuation, and efficiency properties of various IMEX schemes are compared in [Appendix D](#). Simulations of compressible RTI must handle sharp density gradients, extreme stratification, and strong acoustic (shock) waves, which can lead to a highly stiff system. Thus, L-stability, which ensures maximum attenuation, is a vital characteristic when choosing a time integration scheme. Furthermore, total variation diminishing (TVD) ERK methods, which preserve monotonicity even in the presence of shock waves, can be used within the IMEX framework or as an independent explicit time integration scheme. Thus, the optimal time integration methodology for the simulation of compressible RTI, which is used for all of the simulations presented here, is to apply the third-order TVD ERK scheme,

$$\mathbf{U}^* = \mathbf{U}^n + \Delta t \mathbf{F}^n, \quad (78)$$

$$\mathbf{U}^{**} = \mathbf{U}^n + \frac{\Delta t}{4} [\mathbf{F}^n + \mathbf{F}^*], \quad (79)$$

$$\mathbf{U}^{n+1} = \mathbf{U}^n + \frac{\Delta t}{6} [\mathbf{F}^n + \mathbf{F}^* + 4\mathbf{F}^{**}], \quad (80)$$

only when the viscous and diffusion stability requirements are less strict than the convective-acoustic CFL restriction. The syntax for the presentation of the time integration schemes is discussed in [Appendix B](#). When the time step required to explicitly handle the diffusive terms becomes less than the time step necessary to satisfy the CFL stability condition, a second-order IMEX scheme is employed, such that the convective-acoustic time step can be used. The same three-stage TVD ERK scheme from (78)–(80) is combined with a three-stage, L-stable DIRK method as,

$$\mathbf{U}^* = \mathbf{U}^n + \Delta t [\mathbf{H}^n + \mathbf{P}^*], \quad (81)$$

$$\mathbf{U}^{**} = \mathbf{U}^n + \frac{\Delta t}{4} [\mathbf{H}^n + \mathbf{H}^* - 2\mathbf{P}^* + 4\mathbf{P}^{**}], \quad (82)$$

$$\mathbf{U}^{n+1} = \mathbf{U}^n + \frac{\Delta t}{6} [\mathbf{H}^n + \mathbf{H}^* + 4\mathbf{H}^{**} - 6\mathbf{P}^* + 6\mathbf{P}^{**} + 6\mathbf{P}^{n+1}]. \quad (83)$$

Utilizing the same ERK method for both the fully explicit and IMEX schemes simplifies the implementation of the dynamic time integration methodology.

7. Validation of the methodology

A previous study of the incompressible case has shown that PAWCM successfully captures the linear regime, bubble and spike formations, and late-time flow characteristics for the single-mode perturbation case [49]. An extension of that study is presented here, as a feasibility study on the efficacy of the advanced computational framework, presented in the preceding sections, for simulations of compressible RTI. First, a resolution study is performed to give the threshold parameter, ϵ , that corresponds to a converged solution for the compressible RTI system. Then, late-time results are presented for a wide range of flow compressibility and variable density effects. Finally, the flow compressibility effects on the low- A system are shown to match the predictions from linear stability analysis.

7.1. Resolution study

Traditionally, the resolution studies for PAWCM are performed by increasing and decreasing the threshold parameter, ϵ , while adjusting the maximum level of resolution and the number of wavelets used to represent the solution. Since the RTI simulations are initialized with an interface that is as sharp as the grid will allow, all available levels of resolution are initially filled. After the interface has diffused, wavelets on the higher levels of resolution may be left out of the solution. Thus, the resolution convergence study is presented in two ways. First, the threshold parameter, ϵ , is varied with a fixed maximum level of resolution, and the value for ϵ corresponding to a converged solution is found. Then, in order to ensure that the maximum level of resolution is sufficient, a second resolution study is performed by increasing and decreasing the effective resolution, while holding ϵ constant at the optimal value obtained from the first convergence study.

As seen in [Fig. 13](#), the lines corresponding to the $\epsilon = 10^{-3}$ and $\epsilon = 10^{-4}$ cases lie on top of one another. Thus, the solution is assumed to be converged at $\epsilon = 10^{-3}$. The variability for $\epsilon = 10^{-2}$ is small, but noticeable. The threshold parameter is set to $\epsilon = 10^{-3}$ for all other cases presented in this paper.

When the maximum level, J , is increased by one, the effective resolution increases by a factor of two in each dimension. The results of the resolution study for the $A = 0.7$ case are presented in [Fig. 14](#). The solution is assumed converged with a maximum level of resolution $J = 6$.

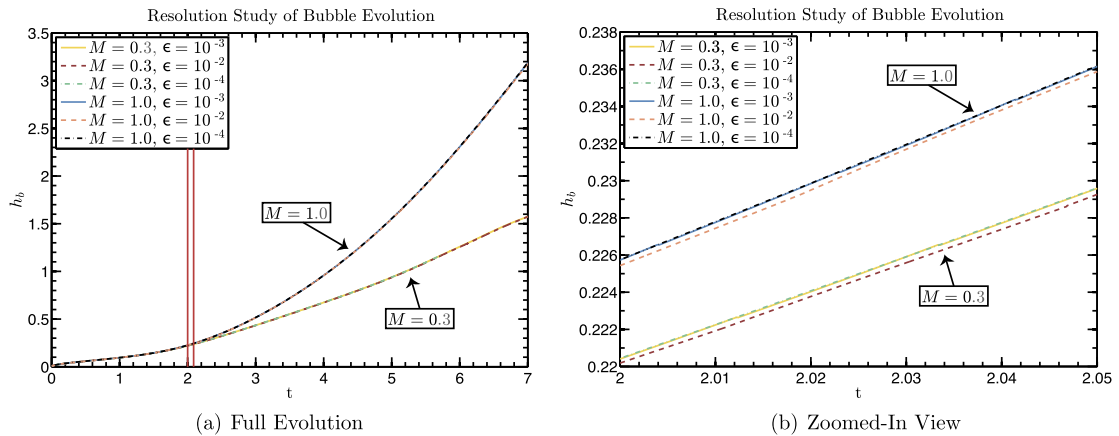


Fig. 13. Resolution convergence study where the threshold parameter ϵ is varied. A zoomed view, corresponding to the region between the two vertical red lines, is presented for clear observation of the line variability for the high- ϵ cases. $A = 0.7$ for all cases. (For interpretation of the references to color in this figure legend, the reader is referred to the web version of this article.)

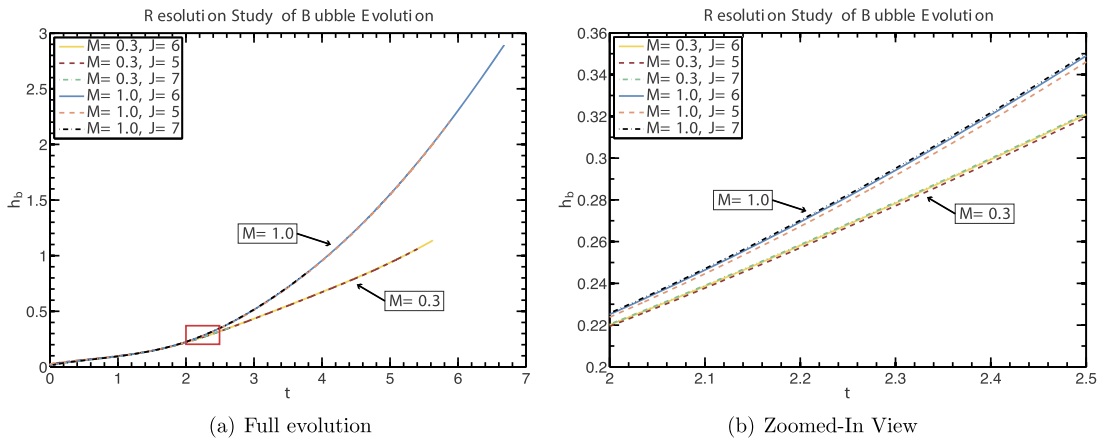


Fig. 14. The results of the resolution study are shown for the entire bubble height evolution, as well as for a small window near the separation of the two bubble height line plots, corresponding to the red box. J is the maximum number of resolution levels. For all cases, $A = 0.7$ and $\epsilon = 10^{-3}$. (For interpretation of the references to color in this figure legend, the reader is referred to the web version of this article.)

7.2. Single-mode 2D compressible RTI simulations

The computational framework combining PAWCM with the consistent initialization, non-reflecting boundary conditions, and dynamic time integration is used to perform DNS of two-dimensional single-mode compressible RTI for a wide range of M and A . The mole fraction at late-times for a selection of cases is shown in Fig. 15. With the addition of the symmetry check during the grid adaptation stages of PAWCM, the solution for all of the cases remain symmetric well into the late-time chaotic growth, even though the interaction among vortices and the induced motions dominate the flow. The four cases shown in the figure highlight the effectiveness of the numerical methodology to capture the wide range of qualitative behavior that characterizes RTI as flow compressibility and variable density effects are modified. For example, finer vortical structures occur at higher A , and large values of M produce narrower spikes due to the steeper background stratification. Whereas the acoustic generation from the initial conditions is minimized, any acoustic disturbances that reach the top or bottom boundaries are efficiently removed from the computational domain.

7.3. Flow compressibility effects at low Atwood number

As a final test for the numerical methodology, the effects of flow compressibility, at fixed material properties, on the system with a small interfacial density difference are examined. A summary of results is given in Fig. 16, where bubble height, spike height, bubble velocity, and spike velocity are shown for various M values for $A = 0.1$ and $Re = 16500$, where the kinematic viscosity is held constant and $Re = \sqrt{g\lambda^3/\nu^2}$. In all cases, an early diffusive regime is followed by an exponential growth phase. Once the bubble and spike structures begin approaching the velocities predicted by potential flow theory as given in (1), they experience a deceleration as vortical structures are created along the interface. The vortex pair interacts with the bubbles and spikes and induces motion to reaccelerate the instability growth. The late time growth varies considerably from the potential flow description, which is obvious from the cases considered here.

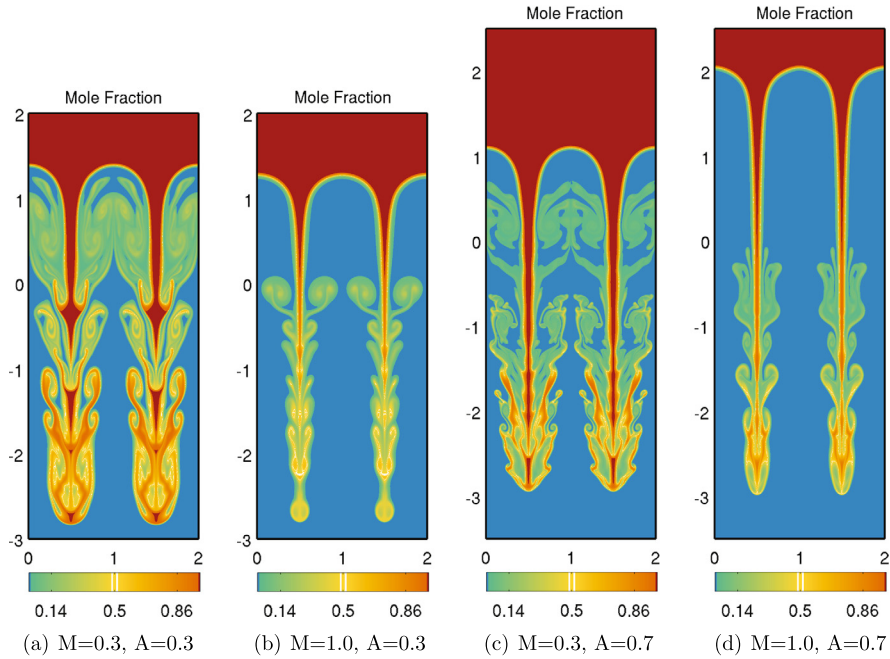


Fig. 15. Mole fraction during late-time RTI growth for a wide range of flow compressibility (M) and variable density (A) effects. The solution for all of the cases remain symmetric well into late times.

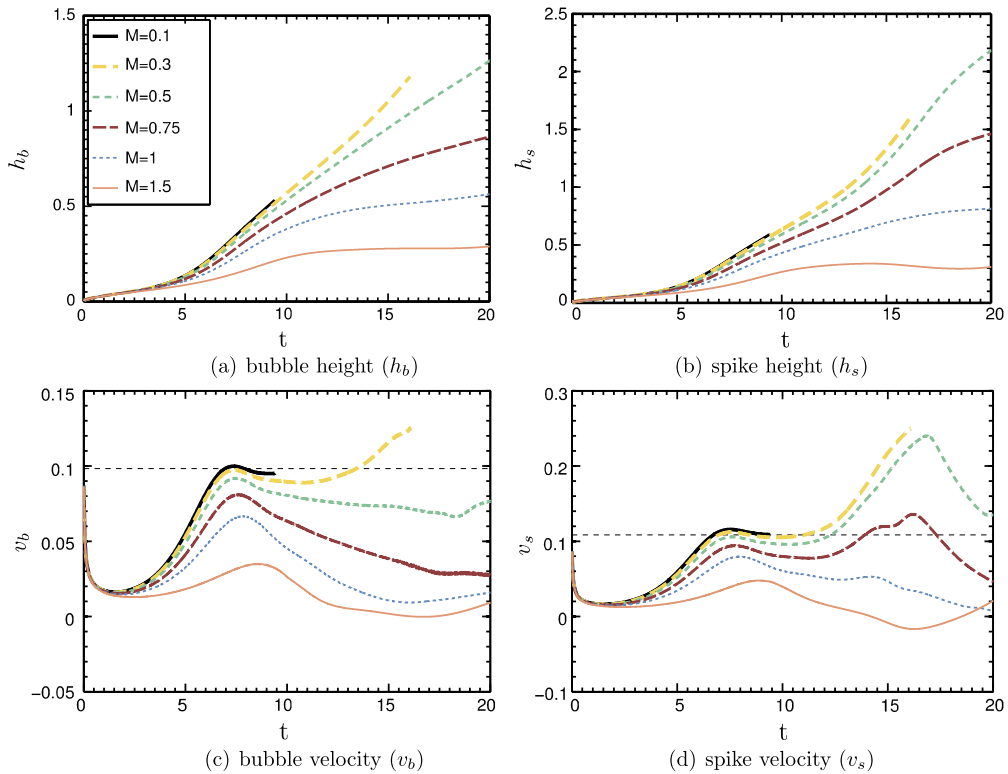


Fig. 16. The M -dependence of the evolutions of bubble height (h_b), spike height (h_s), bubble velocity (v_b), and spike velocity (v_s). The dotted line represents the asymptotic velocity values from potential flow theory.

For the low- A case, increasing the flow compressibility (increasing M) results in a drastic decrease in the overall growth on both the bubble and spike sides of the interface. The M -dependence on the exponential growth observed in the simulations is predicted from linear stability analysis [11]. The behavioral differences observed in the exponential growth regime

extend to the later stages. The decrease in the linear growth as M increases leads to a decrease in the transitional constant bubble velocity, and an overall suppression of the instability growth. The behavior observed for the bubble side is qualitatively the same on the spike side of the interface. However, a stronger reacceleration region occurs for the spike, which may lead to a faster transition to a late-time chaotic development at large Reynolds numbers. For small molar mass differences, when the initial conditions are in thermal equilibrium, flow compressibility and stratification act to suppress the growth of RTI. Out-of-equilibrium initial conditions and fluid compressibility effects will be addressed separately.

8. Conclusions

Simulations of compressible Rayleigh–Taylor systems require the development and implementation of computational tools that efficiently handle acoustic waves, extreme density ranges, and a wide array of physical scales. These difficulties are successfully dealt with by the use of PAWCM in conjunction with two different, but equally effective, boundary treatments that successfully remove acoustic disturbances from the computational domain. The use of PAWCM for direct numerical simulations of Rayleigh–Taylor systems is efficient, since the spatial localization of the mixing layer leads to significant compression in the number of wavelets necessary to accurately represent the flow, while maintaining a high effective resolution and an explicit error control. The first boundary method applies a buffer zone near the vertical edges, where strong numerical diffusion is applied. The use of a dynamically adaptive grid allows the diffusion zone to be extended to extreme lengths, which ensures maximum damping of the acoustic waves with negligible added computational cost. The second method utilizes characteristic analysis to apply a non-reflecting boundary condition that removes the energy in the acoustic waves from the system at the domain boundaries. The analysis takes into account the background stratification present in compressible Rayleigh–Taylor systems. The generation of acoustic waves during the initialization is limited by reducing the pressure disturbances near the interface, which further improves the use of computational resources. All aspects of the advanced computational framework presented here can easily be extended to the multi-mode system, to three-dimensional simulations, and for use with any Adaptive Mesh Refinement (AMR) method.

The advanced computational framework developed specifically for direct numerical simulations of compressible Rayleigh–Taylor systems is likely to shed new light on the nature of the RTI. The compressibility effects cannot be summarized by any one single quantity, nor are the effects universal. Stratification is closely tied to the intrinsic compressibility within the system when the initial conditions are in thermal equilibrium, but it is also affected by the molar mass difference between the two fluids. The two effects can be completely decoupled for thermal out-of-equilibrium initial conditions. When the molar mass difference is small, the background stratification acts to suppress the instability growth, and global stability can be achieved quickly. However, when there is a large difference in molar mass, unstable configurations within a highly compressive system may lead to an enhanced growth when compared to the incompressible system. Such results may have important applications to understanding the mixing in the ICF context.

For the incompressible configuration, recent results paint a completely new picture for the instability growth, which is governed by a new growth mechanism than previously believed [18]. The simulations presented here seem to indicate that this mechanism is still present in the compressible case. However, its effects may be amplified or reduced depending on the background stratification (which can be further increased in complexity with out-of-equilibrium initial conditions), flow and material compressibility, and Atwood number. These simulations need to be extended to higher resolutions in order to achieve the large Reynolds numbers required to understand the true late-time behavior of the compressible single-mode case. The related effects on the multi-mode case remain outstanding open questions. The high-resolution simulations needed to answer these questions are not possible on today's computers, unless specialized computational strategies are used, such as those introduced in this paper.

Acknowledgements

This work was made possible by funding from the LDRD program at Los Alamos National Laboratory through project numbers 20070195ER and 20090058DR. OVV and SJR were supported by Los Alamos National Laboratory, under subcontract No 57206-001-07. This support is gratefully acknowledged. Computational resources were provided by the LANL Institutional Computing (IC) Program.

Appendix A. Local one-dimensional inviscid (LODI) relations for stratified flow

For waves that are approximately planar, traveling along the x_1 -axis, the analysis is simplified by considering the one-dimensional Euler equations,

$$\frac{\partial \rho}{\partial t} + \rho \frac{\partial u_1}{\partial x_1} + u_1 \frac{\partial \rho}{\partial x_1} = 0, \quad (\text{A.1})$$

$$\frac{\partial u_1}{\partial t} + u_1 \frac{\partial u_1}{\partial x_1} + \frac{1}{\rho} \frac{\partial p}{\partial x_1} = 0, \quad (\text{A.2})$$

$$\frac{\partial p}{\partial t} + \rho c^2 \frac{\partial u_1}{\partial x_1} + u_1 \frac{\partial p}{\partial x_1} = 0, \quad (\text{A.3})$$

where $c = \sqrt{\gamma p / \rho}$ is the speed of sound. After decomposing pressure and density into the steady hydrostatic background state and the unsteady fields as in (45)–(46), the modified Euler equations are

$$\frac{\partial \check{\rho}}{\partial t} + \rho \frac{\partial u_1}{\partial x_1} + u_1 \frac{\partial \check{\rho}}{\partial x_1} = -u_1 \frac{\partial \rho^H}{\partial x_1}, \quad (\text{A.4})$$

$$\frac{\partial u_1}{\partial t} + u_1 \frac{\partial u_1}{\partial x_1} + \frac{1}{\rho} \frac{\partial \check{p}}{\partial x_1} = \frac{\rho^H g}{\rho}, \quad (\text{A.5})$$

$$\frac{\partial \check{p}}{\partial t} + \rho c^2 \frac{\partial u_1}{\partial x_1} + u_1 \frac{\partial \check{p}}{\partial x_1} = \rho^H g u_1, \quad (\text{A.6})$$

where the terms that have been added to the classical LODI analysis to account for stratification are colored blue (for clarity of the terms colored blue, the reader is referred to the web version of this article). The differential characteristic variables for this system are

$$\delta v_1 = \rho c \delta u_1 - \delta \check{p}, \quad (\text{A.7})$$

$$\delta v_2 = c^2 \delta \check{\rho} - \delta \check{p}, \quad (\text{A.8})$$

$$\delta v_3 = \rho c \delta u_1 + \delta \check{p}, \quad (\text{A.9})$$

which results with the following characteristic equations:

$$\frac{\partial v_1}{\partial t} + (u_1 - c) \frac{\partial v_1}{\partial x} = -(u_1 - c) \rho^H g, \quad (\text{A.10})$$

$$\frac{\partial v_2}{\partial t} + u_1 \frac{\partial v_2}{\partial x} = u_1 (\gamma - 1) \rho^H g, \quad (\text{A.11})$$

$$\frac{\partial v_3}{\partial t} + (u_1 + c) \frac{\partial v_3}{\partial x} = (u_1 + c) \rho^H g. \quad (\text{A.12})$$

Therefore, the LODI relations are applied only to the unsteady fields, with the hydrostatic background state affecting the system through appropriate source terms in the characteristic equations. The characteristic equations are all of the form

$$\frac{\partial v_\kappa}{\partial t} + \lambda_\kappa \frac{\partial v_\kappa}{\partial x_1} = S_\kappa, \quad (\text{A.13})$$

where λ_κ are the characteristic velocities, and S_κ are the source terms. Each equation can be rewritten as

$$\frac{\partial v_\kappa}{\partial t} + \mathcal{I}_\kappa = S_\kappa, \quad (\text{A.14})$$

where the \mathcal{I}_κ correspond to the time variations of the characteristic wave amplitudes after removing the stratified background, given by

$$\mathcal{I}_1 = \lambda_1 \left(\frac{\partial \check{p}}{\partial x_1} - \rho c \frac{\partial u_1}{\partial x_1} \right), \quad (\text{A.15})$$

$$\mathcal{I}_2 = \lambda_2 \left(c^2 \frac{\partial \check{\rho}}{\partial x_1} - \frac{\partial \check{p}}{\partial x_1} \right), \quad (\text{A.16})$$

$$\mathcal{I}_3 = \lambda_3 \left(\frac{\partial \check{p}}{\partial x_1} + \rho c \frac{\partial u_1}{\partial x_1} \right), \quad (\text{A.17})$$

with characteristic velocities

$$\lambda_1 = u_1 - c, \quad (\text{A.18})$$

$$\lambda_2 = u_1, \quad (\text{A.19})$$

$$\lambda_3 = u_1 + c. \quad (\text{A.20})$$

The primitive variables can now be written in terms of the amplitude variations of the characteristic waves as

$$\frac{\partial \rho}{\partial t} + \frac{1}{2c^2} (\mathcal{I}_3 + \mathcal{I}_1 + 2\mathcal{I}_2) = -u_1 \frac{\partial \rho^H}{\partial x_1}, \quad (\text{A.21})$$

$$\frac{\partial u_1}{\partial t} + \frac{1}{2\rho c} (\mathcal{I}_3 - \mathcal{I}_1) = \frac{\rho^H g}{\rho}, \quad (\text{A.22})$$

$$\frac{\partial p}{\partial t} + \frac{1}{2} (\mathcal{I}_3 + \mathcal{I}_1) = \rho^H g u_1. \quad (\text{A.23})$$

Appendix B. Implicit time integration schemes

Implicit time integration schemes are commonly utilized to solve the full Navier–Stokes equations, where diffusion is important. This avoids any restriction placed on the size of the time-step for high resolution simulations, which must be considered when using an explicit time discretization. The simplified governing equations from (39) can be discretized using the Crank–Nicholson method as,

$$\frac{\mathbf{U}^{n+1} - \mathbf{U}^n}{\Delta t} = \frac{1}{2} [\mathbf{F}^n + \mathbf{F}^{n+1}], \quad (\text{B.1})$$

where the superscripted quantities, \mathbf{U}^n and \mathbf{U}^{n+1} , represent the solution at the beginning and end, respectively, of the current time step. Also, the terms on the right-hand side of the equation represent the evaluation of $\mathbf{F}(\mathbf{U})$ at the appropriate time level, that is $\mathbf{F}^n \equiv \mathbf{F}(\mathbf{U}^n)$. The Crank–Nicholson method is unconditionally stable and second-order accurate, that is, $O(\Delta t^2)$. For systems where higher accuracy is needed, preconditioned Krylov-subspace solvers are often used. Implicit methods often use a linearization of the discretized equations and require an iterative scheme, such as the preconditioned biconjugate gradient stabilized (BiCGSTAB) method, to handle nonlinearity in the system. When PAWCM is used, a multilevel method, similar to the multigrid method but on an adaptive grid, can optimize the iterative process within the BiCGSTAB method. However, for highly nonlinear systems, where the hyperbolic terms in the governing equations are significant, the convergence of the iterative process is not predictable, making the use of implicit time integration methods inefficient.

Appendix C. Explicit time integration schemes

When using explicit schemes, the Courant–Friedrichs–Lewy (CFL) stability condition must be satisfied when nonlinearities in the system are significant. The convective-acoustic CFL condition is

$$\frac{(U + c)\Delta t}{\Delta x} \leq C, \quad (\text{C.1})$$

where U is the local absolute fluid velocity, c is the local speed of sound, and C is the CFL coefficient that depends on the discretization scheme. Typically, $C \leq 1$, where the maximum allowed time step size is directly proportional to C . For cases where the CFL condition is stricter than any of the diffusion stability requirements when setting the time step size, explicit time integration schemes are the optimal choice. The fully explicit Runge–Kutta (ERK) scheme,

$$\mathbf{U}^* = \mathbf{U}^n + \Delta t \mathbf{F}^n, \quad (\text{C.2})$$

$$\mathbf{U}^{n+1} = \frac{1}{2} \mathbf{U}^n + \frac{1}{2} \mathbf{U}^* + \frac{1}{2} \Delta t \mathbf{F}^*, \quad (\text{C.3})$$

where \mathbf{U}^* represents the solution at an intermediate time level, is second-order accurate, that is $O(\Delta t^2)$, and total variation diminishing (TVD) [50]. TVD schemes are successful at simulating the propagation of shock waves while preserving monotonicity. A TVD time integration scheme is a good choice for simulations of compressible RTI, due to the presence of sharp acoustic waves, especially when the molar mass difference is large and the stratification is strong. The second-order TVD Runge–Kutta scheme can also be written as

$$\mathbf{U}^* = \mathbf{U}^n + \Delta t \mathbf{F}^n, \quad (\text{C.4})$$

$$\mathbf{U}^{n+1} = \mathbf{U}^n + \frac{\Delta t}{2} [\mathbf{F}^n + \mathbf{F}^*]. \quad (\text{C.5})$$

A third-order, that is $O(\Delta t^3)$, fully explicit TVD Runge–Kutta scheme is

$$\mathbf{U}^* = \mathbf{U}^n + \Delta t \mathbf{F}^n, \quad (\text{C.6})$$

$$\mathbf{U}^{**} = \frac{3}{4} \mathbf{U}^n + \frac{1}{4} \mathbf{U}^* + \frac{1}{4} \Delta t \mathbf{F}^*, \quad (\text{C.7})$$

$$\mathbf{U}^{n+1} = \frac{1}{3} \mathbf{U}^n + \frac{2}{3} \mathbf{U}^{**} + \frac{2}{3} \Delta t \mathbf{F}^{**}, \quad (\text{C.8})$$

where \mathbf{U}^* and \mathbf{U}^{**} are the solutions at intermediate time levels [50]. This scheme has a low storage requirement because the evaluations of $\mathbf{F}(\mathbf{U})$ are always taken at the current intermediate time level. The third-order TVD ERK scheme can also be written as shown in (78)–(80). Both of the TVD ERK schemes have a CFL coefficient of unity.

Appendix D. Implicit–explicit time integration schemes

A single-stage DIRK scheme is combined with a two-stage ERK method to form a second-order IMEX scheme as [48],

$$\mathbf{U}^* = \mathbf{U}^n + \frac{\Delta t}{2} [\mathbf{H}^n + \mathbf{P}^*], \quad (\text{D.1})$$

$$\mathbf{U}^{n+1} = \mathbf{U}^n + \Delta t [\mathbf{H}^* + \mathbf{P}^*]. \quad (\text{D.2})$$

Applying the test equation, $\partial U / \partial t = \lambda U$, to this DIRK method, with $z = \lambda \Delta t$, the convergence factor in the stiffness limit of $z \rightarrow -\infty$ is $R(\infty) = 1$, which corresponds to no attenuation. However, the scheme is A-stable, since $|R(z)| \leq 1$ for $\text{Re}(z) \leq 0$.

A similar second-order IMEX scheme can be derived by combining the two-stage TVD ERK method from (C.4)–(C.5) with a Crank–Nicholson single-stage implicit method as,

$$\mathbf{U}^* = \mathbf{U}^n + \frac{\Delta t}{2} [2\mathbf{H}^n + \mathbf{P}^n + \mathbf{P}^*], \quad (\text{D.3})$$

$$\mathbf{U}^{n+1} = \mathbf{U}^n + \frac{\Delta t}{2} [\mathbf{H}^n + \mathbf{P}^n + \mathbf{H}^* + \mathbf{P}^*]. \quad (\text{D.4})$$

Whereas this combination has the benefits of a TVD explicit scheme and an A-stable implicit scheme, there is no attenuation in the stiffness limit.

A third-order IMEX scheme using a two-stage, A-stable DIRK and a three-stage ERK method is [48],

$$\mathbf{U}^* = \mathbf{U}^n + \Delta t \gamma [\mathbf{H}^n + \mathbf{P}^*], \quad (\text{D.5})$$

$$\mathbf{U}^{**} = \mathbf{U}^n + \Delta t [(\gamma - 1)(\mathbf{H}^n - 2\mathbf{H}^*) + (1 - 2\gamma)\mathbf{P}^* + \mathbf{P}^{**}], \quad (\text{D.6})$$

$$\mathbf{U}^{n+1} = \mathbf{U}^n + \frac{\Delta t}{2} [\mathbf{H}^* + \mathbf{P}^* + \mathbf{H}^{**} + \mathbf{P}^{**}], \quad (\text{D.7})$$

where $\gamma = (3 + \sqrt{3})/6$. This method has some attenuation of the stability function in the stiffness limit, since $|R(\infty)| = 0.7321$.

The three-stage TVD ERK scheme from (78)–(80) is combined with a two-stage DIRK method to produce a second-order IMEX scheme as,

$$\mathbf{U}^* = \mathbf{U}^n + \Delta t [\mathbf{H}^n + \mathbf{P}^*], \quad (\text{D.8})$$

$$\mathbf{U}^{**} = \mathbf{U}^n + \frac{\Delta t}{4} [\mathbf{H}^n + \mathbf{H}^* - 2\mathbf{P}^* + 4\mathbf{P}^{**}], \quad (\text{D.9})$$

$$\mathbf{U}^{n+1} = \mathbf{U}^n + \frac{\Delta t}{6} [\mathbf{H}^n + \mathbf{H}^* + 4\mathbf{H}^{**} + 6\mathbf{P}^{**}]. \quad (\text{D.10})$$

The attenuation is even stronger with this A-stable method, since $|R(\infty)| = 0.5$.

For highly-stiff problems, it is important that the discretization is L-stable, which combines A-stability with full attenuation in the stiffness limit, that is $|R(\infty)| = 0$. A second-order IMEX scheme that combines a two-stage, L-stable DIRK and a three-stage ERK method is [48],

$$\mathbf{U}^* = \mathbf{U}^n + \Delta t \gamma [\mathbf{H}^n + \mathbf{P}^*], \quad (\text{D.11})$$

$$\mathbf{U}^{**} = \mathbf{U}^n + \Delta t [\delta \mathbf{H}^n + (1 - \delta)\mathbf{H}^* + (1 - \gamma)\mathbf{P}^* + \gamma \mathbf{P}^{**}], \quad (\text{D.12})$$

$$\mathbf{U}^{n+1} = \mathbf{U}^n + \Delta t [(1 - \gamma)(\mathbf{H}^* + \mathbf{P}^*) + \gamma(\mathbf{H}^{**} + \mathbf{P}^{**})], \quad (\text{D.13})$$

where $\gamma = (2 - \sqrt{2})/2$ and $\delta = -2\sqrt{2}/3$.

The previous IMEX schemes all include an additional explicit step following the final implicit stage. Identifying the last internal stage with the solution at the next time step ensures L-stability and is particularly good for highly-stiff problems. A second-order IMEX scheme using a two-stage, L-stable DIRK scheme and a two-stage ERK method is [48],

$$\mathbf{U}^* = \mathbf{U}^n + \Delta t \gamma [\mathbf{H}^n + \mathbf{P}^*], \quad (\text{D.14})$$

$$\mathbf{U}^{n+1} = \mathbf{U}^n + \Delta t [\delta \mathbf{H}^n + (1 - \delta)\mathbf{H}^* + (1 - \gamma)\mathbf{P}^* + \gamma \mathbf{P}^{n+1}], \quad (\text{D.15})$$

where $\gamma = (2 - \sqrt{2})/2$ and $\delta = 1 - 1/(2\gamma)$.

A second-order IMEX method results from the combination of the three-stage TVD ERK scheme from (78)–(80) and a three-stage, L-stable DIRK method as shown in (81)–(83). The cost of an additional implicit step should be weighed against the need of a TVD explicit method and an L-stable implicit scheme.

References

- [1] L. Rayleigh, Investigation of the character of the equilibrium of an incompressible heavy fluid of variable density, Proc. R. Math. Soc. 14 (1883) 170–177.
- [2] G. Taylor, The instability of liquid surfaces when accelerated in a direction perpendicular to their planes, Proc. R. Soc. Lond. Ser. A 201 (1950) 192–196.
- [3] B.A. Remington, S.V. Weber, M.M. Marinak, S.W. Haan, J.D. Kilkenny, R.J. Wallace, G. Dimonte, Single-mode and multi-mode Rayleigh–Taylor experiments on NOVA, Phys. Plasmas 2 (1995) 241–255.
- [4] D.R. Farley, L.M. Logory, Single-mode, nonlinear mix experiments at high Mach number using Nova, Astrophys. J. Suppl. Ser. 127 (2000) 311–316.

- [5] D. Livescu, Numerical simulations of two-fluid turbulent mixing at large density ratios and applications to the Rayleigh–Taylor instability, *Philos. Trans. R. Soc. A* 371 (2013) 20120185, <http://dx.doi.org/10.1098/rsta.2012.0185>.
- [6] J.D. Kilkenny, S.G. Glendinning, S.W. Haan, B.A. Hammel, J.D. Lindl, D. Munro, B.A. Remington, S.V. Weber, J.P. Knauer, C.P. Verdon, A review of the ablative stabilization of the Rayleigh–Taylor instability in regimes relevant to inertial confinement fusion, *Phys. Plasmas* 1 (1994) 1379–1389.
- [7] J.P. Knauer, R. Betti, D.K. Bradley, T.R. Boehly, T.J.B. Collins, V.N. Goncharov, P.W. McKenty, D.D. Meyerhofer, V.A. Smalyuk, C.P. Verdon, S.G. Glendinning, D.H. Kalantar, R.G. Watt, Single-mode, Rayleigh–Taylor growth-rate measurements on the OMEGA laser system, *Phys. Plasmas* 7 (2000) 338–345.
- [8] G.C. Jordan IV, R.T. Fisher, D.M. Townsley, A.C. Calder, C. Graziani, S. Asida, D.Q. Lamb, J.W. Truran, Three-dimensional simulations of the deflagration phase of the gravitationally confined detonation model of type Ia supernovae, *Astrophys. J. Lett.* 681 (2008) 1448.
- [9] W.H.G. Lewin, J. van Paradijs, E.P.J. van den Heuvel, X-ray Binaries, Cambridge University Press, Cambridge, UK, 1995.
- [10] J.M. Blondin, D.C. Ellison, Rayleigh–Taylor instabilities in young supernova remnants undergoing efficient particle acceleration, *Astrophys. J.* 560 (2001) 244–253.
- [11] D. Livescu, Compressibility effects on the Rayleigh–Taylor instability growth between immiscible fluids, *Phys. Fluids* 16 (2004) 118–127.
- [12] S. Gauthier, B. Le Creurer, Compressibility effects in Rayleigh–Taylor instability-induced flows, *Philos. Trans. R. Soc. A* 368 (2010) 1681–1704.
- [13] D. Livescu, J.R. Ristorcelli, R.A. Gore, S.H. Dean, W.H. Cabot, A.W. Cook, High-Reynolds number Rayleigh–Taylor turbulence, *J. Turbul.* 10 (2009) 1–32.
- [14] B.J. Olson, A.W. Cook, Rayleigh–Taylor shock waves, *Phys. Fluids* 19 (2007) 128108.
- [15] D.L. Youngs, Application of monotone integrated large eddy simulation to Rayleigh–Taylor mixing, *Philos. Trans. R. Soc. A* 367 (2009) 2971–2983.
- [16] G. Dimonte, D.L. Youngs, A. Dimits, S. Weber, M. Marinak, S. Wunsch, C. Garasi, A. Robinson, M.J. Andrews, P. Ramaprabhu, A.C. Calder, B. Fryxell, J. Biello, L. Dursi, P. MacNeice, K. Olson, P. Ricker, R. Rosner, F. Timmes, H. Tufo, Y.N. Young, M. Zingale, A comparative study of the turbulent Rayleigh–Taylor instability using high-resolution three-dimensional numerical simulations: the Alpha-Group collaboration, *Phys. Fluids* 16 (2004) 1668–1693.
- [17] S. Gauthier, Compressibility effects in Rayleigh–Taylor flows: influence of the stratification, *Phys. Scr. T* 155 (2013) 014012.
- [18] T. Wei, D. Livescu, Late-time quadratic growth in single-mode Rayleigh–Taylor instability, *Phys. Rev. E* 86 (2012) 046405.
- [19] M.J. Andrews, D.L. Youngs, D. Livescu, T. Wei, Computational studies of two-dimensional Rayleigh–Taylor driven mixing for a tilted-rig, *J. Fluids Eng.* 136 (2014) 091212.
- [20] B. Le Creurer, S. Gauthier, A return toward equilibrium in a 2D Rayleigh–Taylor instability for compressible fluids with a multidomain adaptive Chebyshev method, *Theor. Comput. Fluid Dyn.* 22 (2008) 125–144.
- [21] K. Schneider, O.V. Vasilyev, Wavelet methods in computational fluid dynamics, *Annu. Rev. Fluid Mech.* 42 (2010) 473–503.
- [22] S. Chandrasekhar, Hydrodynamic and Hydromagnetic Stability, Dover, New York, 1981.
- [23] R.E. Duff, F.H. Harlow, C.W. Hirt, Effects of diffusion on interface instability between gases, *Phys. Fluids* 5 (1962) 417–425.
- [24] V.N. Goncharov, Analytical model of nonlinear, single-mode, classical Rayleigh–Taylor instability at arbitrary Atwood numbers, *Phys. Rev. Lett.* 88 (2002) 134502.
- [25] D. Oron, L. Arazi, D. Kartoon, A. Rikanati, U. Alon, D. Shvarts, Dimensionality dependence of the Rayleigh–Taylor and Richtmyer–Meshkov instability late-time scaling laws, *Phys. Plasmas* 8 (2001) 2883–2889.
- [26] F.A. Williams, Combustion Theory, Benjamin/Cummings, Menlo Park, 1985.
- [27] H. Yu, D. Livescu, Rayleigh–Taylor instability in cylindrical geometry with compressible fluids, *Phys. Fluids* 20 (2008) 104103.
- [28] M. Farge, K. Schneider, Coherent vortex simulation (CVS), a semi-deterministic turbulence model using wavelets, *Flow Turbul. Combust.* 66 (2001) 393–426.
- [29] B. Hejiazalhosseini, D. Rossinelli, M. Bergdorf, P. Koumoutsakos, High order finite volume methods on wavelet-adapted grids with local time-stepping on multicore architectures for the simulation of shock-bubble interactions, *J. Comput. Phys.* 229 (2010) 8364–8383.
- [30] S. Paolucci, Z.J. Zikoski, D. Wirasaet, WAMR: an adaptive wavelet method for the simulation of compressible reacting flow. Part I. Accuracy and efficiency of algorithm, *J. Comput. Phys.* 272 (2014) 814–841, <http://dx.doi.org/10.1016/j.jcp.2014.01.025>.
- [31] S. Paolucci, Z.J. Zikoski, T. Grenga, WAMR: an adaptive wavelet method for the simulation of compressible reacting flow. Part II. The parallel algorithm, *J. Comput. Phys.* 272 (2014) 842–864, <http://dx.doi.org/10.1016/j.jcp.2014.03.059>.
- [32] A. Nejadmalayeri, A. Vezolainen, E. Brown-Dymkoski, O.V. Vasilyev, Parallel adaptive wavelet collocation method for PDEs, *J. Comput. Phys.* 298 (2015) 237–253, <http://dx.doi.org/10.1016/j.jcp.2015.05.028>.
- [33] O.V. Vasilyev, Solving multi-dimensional evolution problems with localized structures using second generation wavelets, *Int. J. Comput. Fluid Dyn.* 17 (2003) 151–168.
- [34] O.V. Vasilyev, C. Bowman, Second-generation wavelet collocation method for the solution of partial differential equations, *J. Comput. Phys.* 165 (2000) 660–693.
- [35] O.V. Vasilyev, S. Paolucci, A fast adaptive wavelet collocation algorithm for multidimensional PDEs, *J. Comput. Phys.* 138 (1997) 16–56.
- [36] N.K.R. Kevlahan, O.V. Vasilyev, An adaptive wavelet collocation method for fluid–structure interaction at high Reynolds numbers, *SIAM J. Sci. Comput.* 26 (2005) 1894–1915.
- [37] S.M. Reckinger, O.V. Vasilyev, B. Fox-Kemper, Adaptive volume penalization for ocean modeling, *Ocean Dyn.* 62 (2012) 1201–1215.
- [38] Q. Liu, O.V. Vasilyev, A Brinkman penalization method for compressible flows in complex geometries, *J. Comput. Phys.* 227 (2007) 946–966.
- [39] J.D. Regele, O.V. Vasilyev, An adaptive wavelet-collocation method for shock computations, *Int. J. Comput. Fluid Dyn.* 23 (2009) 503–518.
- [40] W. Sweldens, The lifting scheme: a construction of second generation wavelets, *SIAM J. Math. Anal.* 29 (1998) 511–546.
- [41] X.Y. Hu, B.C. Khoo, N.A. Adams, F.L. Huang, A conservative interface method for compressible flows, *J. Comput. Phys.* 219 (2006) 553–578.
- [42] A.W. Cook, Enthalpy diffusion in multicomponent flows, *Phys. Fluids* 21 (2009) 055109.
- [43] D.D. Joseph, Fluid dynamics of two miscible liquids with diffusion and gradient stresses, *Eur. J. Mech. B, Fluids* 6 (1990) 565–596.
- [44] T. Colonius, Modeling artificial boundary conditions for compressible flow, *Annu. Rev. Fluid Mech.* 36 (2004) 315–345.
- [45] Q. Liu, O.V. Vasilyev, Nonreflecting boundary conditions based on nonlinear multidimensional characteristics, *Int. J. Numer. Methods Fluids* 62 (2010) 24–55.
- [46] T.J. Poinsot, S.K. Lele, Boundary-conditions for direct simulations of compressible viscous flows, *J. Comput. Phys.* 101 (1992) 104–129.
- [47] K.W. Thompson, Time dependent boundary conditions for hyperbolic systems, *J. Comput. Phys.* 68 (1987) 1–24.
- [48] U.M. Ascher, S.J. Ruuth, R.J. Spiteri, Implicit–explicit Runge–Kutta methods for time-dependent partial differential equations, *Appl. Numer. Math.* 25 (1997) 151–167.
- [49] S.J. Reckinger, D. Livescu, O.V. Vasilyev, Adaptive wavelet-collocation method simulations of Rayleigh–Taylor instability, *Phys. Scr. T* 142 (2010) 014064.
- [50] C.W. Shu, S. Osher, Efficient implementation of essentially non-oscillatory shock-capturing schemes, *J. Comput. Phys.* 77 (1988) 439–471.